This is the peer-reviewed, final accepted version for American Mineralogist, published by the Mineralogical Society of America.
The published version is subject to change. Cite as Authors (Year) Title. American Mineralogist, in press.
DOI: https://doi.org/10.2138/am-2023-9052. http://www.minsocam.org/

REVISION 2

Raman spectroscopic measurements on San Carlos olivine up to 14 GPa and 800 K: Implication for thermodynamic properties (Word Count: 9457)

Dan Liu[1,2], Haipeng Song[1], Xi Zhu[1], Yu Ye[1]*, Joseph R. Smyth[3], Yancheng Hu[1], Sha Wang[1], Yunfan Miao[1], Yungui Liu[1,4]

[1]State Key Laboratory of Geological Processes and Mineral Resources, China University of Geosciences, Wuhan, 430074, China

[2]Gemmological Institute, China University of Geosciences, Wuhan, 430074, China

[3]Department of Geological Sciences, University of Colorado, Boulder, Colorado, 80309, USA

[4]College of Gems and Materials Technology, Hebei GEO University, Shijiazhuang, 050031, China

*Corresponding author: Yu Ye (yeyu@cug.edu.cn)

Abstract:

Olivine, the most abundant mineral in the upper mantle, plays a key role in controlling the thermodynamic properties in the Earth's and planetary interiors, like the temperature distribution along the adiabatic geotherm. In this study, we conducted simultaneously high-pressure (P) and high-temperature (T) Raman measurements on a San Carlos olivine sample, in an externally-heated diamond anvil cell (DAC). The intrinsic anharmonic parameters, a_i, are calculated as

functions of both pressure and temperature, and the isochoric (C_V) and isobaric (C_P) heat capacities are computed at various P-T conditions with the anharmonic correction, which are important for the heat transport properties. The harmonic heat capacities are C_V = 807.7 J/kg/K and C_P = 815.4 J/kg/K at the ambient condition, with anharmonic contribution of ΔC = 7.9 J/kg/K. Relative to the previous vibrational measurements conducted at high-P or high-T conditions, this simultaneous high-P,T experiment indicates that the anharmonic contribution to heat capacities is overestimated if the anharmonic parameters (a_i) are treated as constants like before. The pressure effect is marginal on the intrinsic anharmonic contribution to thermodynamic properties, whereas it is much more significant on the external anharmonicity (thermal expansivity). The pressure dependence of C_P (dC_P/dP, in J/kg/K/GPa) increases from -3.14 at 300 K to -1.94 at 700 K, and then decreases smoothly to -5.03 at 1800 K. Combining the derived high-P,T capacity with reliable P-V-T equation of state (EOS) for olivine, we further modeled the thermodynamic Grüneisen parameter, $\gamma(P,T)$. The Grüneisen parameter is important for the connection between isothermal and adiabatic compressions of minerals, which can be decreased by approximately 5 % with the anharmonic correction at high temperatures. The modeled adiabatic bulk modulus and bulk sound velocity can be expressed as: $K_S(T,P)$ (GPa) = 127.5(1) + 4.32(5)·P – 0.018(1)·(T-300) and $V_\Phi(T,P)$ (km/s) = 6.22(2) + 0.069(3)·P – [3.74(15)-0.075(13) ·P]·10^{-4}·(T-300). The adiabatic temperature gradient, dT_S/dP, almost independent of pressure, is equal to 13.40(16) and 12.35(16) K/GPa in the harmonic and anharmonic models, respectively. This study provides a useful example for modeling the radial temperature distribution in adiabatic planetary mantles.

Keywords: Olivine; simultaneously high-*P,T* Raman spectra; intrinsic anharmonic parameter; heat capacity; thermodynamic Grüneisen parameter; adiabatic temperature profile

1. Introduction

Olivine, with a typical composition approximately $(Mg_{0.9}Fe_{0.1})_2SiO_4$ (e.g. Agee 1998), is the most abundant mineral in the upper mantle (60 ~ 70 vol.%) above the 410-km seismic discontinuity. It is also an important component in other terrestrial planets, like Mercury and Mars, as well as some asteroids (Sanchez et al. 2014; Namur et al. 2016; Khan et al. 2018). Its thermodynamic properties play a dominant role in the physics and chemistry of the Earth and planetary interiors. For example, temperature is fundamental for modeling the dynamics of the mantle, and the adiabatic *T*-gradient in olivine is the major factor of controlling the geotherm in the upper mantle considering its abundance (Katsura et al. 2010; Katsura 2022). Among the physical parameters related to adiabatic procedures, the thermodynamic Grüneisen parameter (γ) is key for calculating thermal pressures at high temperatures (Brown and McQueen 1986; Huang et al. 2010, 2018), and heat capacities are also important for connecting the thermal transport properties of thermal conductivity and diffusivity (Zhang et al. 2019, 2023).

In order to derive these thermodynamic properties, we need both precise *P*-*V*-*T* EOS and heat capacities at high-*P,T* conditions (Liebfried and Ludwig 1961; Brown and Shankland 1981; Anderson et al. 1991). Quite a few studies have been reported on *P*-*V*-*T* Equations of state (EOSs) for mantle-composition olivines (e.g., Liu and Li 2006; Dorogokupets et al. 2015; Angel et al. 2018; Katsura 2022), among which Angel et al. (2018) gave a thorough review of the existing datasets. Furthermore, vibrational spectra are widely adopted to model high-*T* heat capacities for minerals (e.g. Kieffer 1979, 1980; Hofmeister 1987; Ross and Navrotsky 1987,

1988; Gillet et al. 1991; Liu et al. 2021).

On the other hand, harmonic (or quasi-harmonic) approximation for thermodynamic properties would deviate from reality at high temperatures, since the atomic vibrations inside the lattice structure cannot be simplified as harmonic oscillators any more under such conditions. Then, anharmonicities must be taken into consideration (Stacey and Isaak 2003; Anderson 2007; Stacey and Hodgkinson 2019). There are generally two types of anharmonicities: (1) 'external anharmonicity' arising from asymmetrical bonding (potential) (e.g. Richet et al. 1977), which is associated with the thermal expansion behaviors of minerals; (2) 'intrinsic anharmonicity' describing deviation of the heat capacity C_V from the Dulong-Petit limit at high temperatures (Anderson et al. 1991). For the case of intrinsic anharmonicity, an anharmonic mode parameter, a_i, is introduced to evaluate the magnitude of the anharmonic correction, which is defined as the variation of a vibrational frequency (v_i) with temperature at constant volume. The intrinsic anharmonicity has profound impact on modelling the thermodynamic properties of minerals at high-*P,T* conditions in the Earth's interior, such as the heat capacities (Kieffer 1979; Cynn et al. 1996a, 1996b; Holland and Powell 1998; Wu 2015), equations of state (Oganov and Dorogokupets 2003, 2004; Dorogokupets and Oganov, 2004), as well as equilibrium isotopic fractionations (Polyakov and Kharlashina 1994; Polyakov 1998; Zhu et al. 2019). Previous studies consistently indicated that the reported a_i parameters are negative for many silicates, such as olivine (Gillet et al. 1991, 1997; Liu et al. 2021), clinohumite (Liu et al. 2019b) and garnets in a cubic structure (Gillet et al. 1992), supporting that the anharmonic contribution is positive to the heat capacities.

In this study, we conducted *in situ* Raman measurements on a San Carlos olivine sample at simultaneously high-*P* and high-*T* conditions, taking advantage of an externally-heated diamond

anvil cell. It is noted that previous vibrational spectroscopic measurements on olivine samples were obtained at ambient conditions (Burns and Huggins 1972; Guyot et al. 1986; Kolesov and Tanskaya 1996; Gaisler and Kolesov 2007; Mouri and Enami 2008; Ishibashi et al. 2012; Breitenfeld et al. 2018), or at only high-temperature (P = 0 GPa) or high-pressure (T = 300 K) conditions (Chopelas 1990; Gillet et al. 1991, 1997; Liu and Mernagh 1993; Wang et al. 1993; Hushur et al. 2009; Manghnani et al. 2013; Yang et al. 2015; Santamaria-Perez et al. 2016; Liu et al. 2019a, 2021). Based on this experiment, we can have a systematical check on the pressure effect on thermodynamic properties at high-temperature conditions (including the heat capacities, Grüneisen parameter, and adiabatic P-T profile). Moreover, the anharmonic parameters (a_i) are traditionally simplified as constants, independent of temperature or pressure (e.g., Gillet et al. 1991, 1997; Liu et al. 2021). Taking advantage of this simultaneously high-P,T Raman measurement, we will also examine the pressure and temperature effects on the intrinsic anharmonicity.

2 Experimental Methods

A natural San Carlos olivine sample, from a peridotite rock collected in Arizona, USA, was adopted for this experiment, and the compositional analysis by electron probe microanalyzer (EPMA) gave the formula of $Mg_{1.753(8)}Fe_{0.223(2)}Ni_{0.0064(1)}Ca_{0.0019(2)}Mn_{0.0030(4)}Si_{1.012(6)}O_4$ (approximately $Fo_{89}Fa_{11}$) (Liu et al. 2021). *In situ* Raman spectra at simultaneous high-temperature and high-pressure conditions were carried out on a Horiba LabRAM HR Evolution system, which is equipped with a micro confocal Raman spectrometer and an 1800 line/mm grating. A green beam (λ = 532 nm) was excited from a Nd YAG laser source operated at 20 mW, and the spectrometer was calibrated with a silicon single crystal as reference, whose fundamental

Si-Si stretching mode is detected at 520.4(1) cm^{-1}. A SLM Plan 50× objective lens with long focal distance was utilized to focus the incident laser beam onto the samples.

A pair of 400-μm-culet diamond anvils, with very low fluorescence, was aligned inside an externally-heated BX90-type diamond anvil cell (outer diameter: 5 cm and height: 4.8 cm) (**Fig. S1**). In total, we conducted six runs of high-pressure Raman measurements at temperatures of 300, 400, 500, 600, 700 and 800 K. Taking the run at T = 400 K for example, a rhenium gasket (5×5×0.2 mm^3) was initially pre-indented to a thickness of 35 μm, and a 260-μm-diameter hole was drilled at the center of the indentation as the sample chamber. A selected sample chip (approximately 50-60 μm in diameter), two or three annealed ruby chips (3 μm in diameter) and commercial cubic boron nitride (cBN) crystals (20-30 μm, pressure standard) were loaded in the sample chamber between two NaCl layers, which had been cold compressed to a thickness about 10 μm.

We had utilized Ar and a methanol-ethanol-water mixture as the pressure transmission media before, and found that the pressure was automatedly increased by more than 7 GPa when the temperature was increased from 300 K to 600 K. The thermal pressure was as small as 2 GPa in the solid NaCl media even when the temperature was raised to 800 K. Hence, we chose NaCl as the pressure medium so as to have a good coverage in the pressure-temperature field below 14 GPa (as in the upper mantle). The DAC was typically sealed below 1 GPa, which was measured at ambient temperature.

A pyrophyllite ceramic cylinder (outer diameter: 22 mm, inner diameter: 6.5 mm, height: 4 mm) was placed outside the DAC, and coiled by a Pt wire (in 200 μm diameter) which serves as the external heating source. A K-type thermocouple was placed onto the diamond anvil in the cylinder side, approximately 0.4 mm away from the culet, and temperature was controlled by an

automated controller with an uncertainty within 5 K. The pyrophyllite ceramic was filled with protection gas (98 vol.% Ar + 2 vol.% H_2) throughout the high-temperature measurements to prevent potential oxidation of the diamond anvils at high temperatures. Initially, we increased the temperature up to 800 K and maintained it for 15 minutes, so as to anneal differential stress in the NaCl medium. Weidner et al. (1994) examined the differential stress in NaCl at various pressure-temperature conditions. They found that the differential stress increases steadily to approximately 0.3 GPa around 2 GPa, and remains almost constant at higher pressure at T = 300 K. At P = 6 GPa, the differential stress was observed to decrease rapidly at elevated temperature, and approached 0 GPa above 673 K, under which hydrostatic compression should be achieved inside the DAC chamber. This phenomenon is also observed in the laser-heated DAC experiments, and the annealed differential stress in NaCl was kept within 1 GPa even up to 1 megabar (Dorfman et al. 2010, 2012; Uts et al. 2013). Hence, the differential stress in the NaCl medium is expected to be no more than 0.3 GPa throughout this high-P,T experiment, which is smaller than the measurement uncertainties from the pressure standard.

Next, temperature was decreased to 400 K and the pressure was measured to be 2.4 GPa. Pressure inside the chamber was gradually increased up to 13.1 GPa at intervals of 0.3 – 1.3 GPa, and the temperature was maintained at 400 K throughout this experimental run. In total, 11 Raman spectra were obtained, and each one was collected in the range of 100 – 1200 cm^{-1} with an accumulation of 5 times and a duration of 3 minutes for each time. Noted that the full width at half maxima (FWHM) of ruby R_1 line gets much wider especially above 600 K, causing severe uncertainty in pressure determination. Hence, pressures at high-T conditions were calibrated by the cBN pressure scale (Datchi et al. 2004), which were measured before and after collection of each spectrum with a difference typically within 0.3 GPa. In the following runs at higher

159 temperatures, we pre-indented new Re gaskets, and repeated the experimental procedure
160 mentioned above. The *P*-*T* conditions for our experiment are summarized in **Fig. 1**. On the other
161 hand, Liu et al. (2021) measured high-*T* Raman spectra on this San Carlos olivine sample up to
162 1193 K in a Linkam THMS 1500 heating stage at the ambient pressure, and high-*P* Raman
163 spectra up to 19 GPa in DAC in an Argon pressure medium at room temperature. Noted that
164 these high-*P* Raman spectra collected in NaCl (at T = 300 K) are consistent with the previous
165 ones obtained in Ar throughout this experimental *P*-range below 14 GPa.

166 The software package of Peakfit v4.12 was utilized for the analyses of the Raman spectra
167 including fitting background and distinguishing peaks. In total, 75 Raman spectra were recorded
168 at various *P*-*T* conditions, and up to 10 modes are fitted by Gaussian peak shapes in each
169 spectrum. The phonon-phonon interaction is not so significant to obviously change the peak
170 shapes or symmetry even at high temperatures. The background can be simply treated as a
171 slightly inclined line from 100 to 1100 cm^{-1}, since the spectra were collected through the
172 diamond windows with very low fluorescence.

173

174 **3 Results and discussion**

175 **3.1 Vibrational modes at various *P*-*T* conditions**

176 The $(Mg,Fe)_2SiO_4$ olivine crystallizes in a orthorhombic structure (space group: *Pbnm*)
177 with 4 formula units in a unit cell (Z = 4). Consequently, there are 84 vibrational modes,
178 including 3 acoustic modes and 81 optical modes (Fateley et al. 1971; Farmer and Lazarev 1974;
179 Iishi 1978; Hofmeister 1987; Rao et al. 1988; Chopelas 1991; Kolesov and Geiger 2004). The
180 optical vibrations are further divided into three groups: 36 Raman-active ones (11 A_g + 11 B_{1g} + 7

This is the peer-reviewed, final accepted version for American Mineralogist, published by the Mineralogical Society of America.
The published version is subject to change. Cite as Authors (Year) Title. American Mineralogist, in press.
DOI: https://doi.org/10.2138/am-2023-9052. http://www.minsocam.org/

B_{2g} + 7 B_{3g}), 35 IR-active ones (9 B_{1u} + 13 B_{2u} + 13 B_{3u}), and 10 inactive modes (10A_u). On the other hand, the optical modes can also be divided according to their attributions: (1) 45 lattice vibrations (5 A_g + 5 B_{1g} + 4 B_{2g} + 4 B_{3g} + 7 A_u + 7 B_{1u} + 6 B_{2u} + 7B_{3u}) associated with the translations of Mg^{2+}/Fe^{2+} cations (denoted as T(M)) as well as translations and rotations of SiO_4 units (T(Si) and R(Si), respectively), which are distributed in the frequency range below 482 cm^{-1}; (2) 8 symmetric (v_2, 1 A_g + 1 B_{1g} + 1 B_{2g} + 1 B_{3g} + 1 A_u + 1 B_{1u} + 1 B_{2u} + 1 B_{3u}) and 12 asymmetric (v_4, 2 A_g + 2 B_{1g} + 1 B_{2g} + 1 B_{3g} + 1 A_u + 1 B_{1u} + 2 B_{2u} + 2 B_{3u}) O-Si-O bending modes inside SiO_4 tetrahedra in the range from 349 to 644cm^{-1}; (3) 4 symmetric (v_1, 1 A_g + 1 B_{1g} + 1 B_{2u} + 1 B_{3u}) and 12 asymmetric (v_3, 2 A_g + 2 B_{1g} + 1 B_{2g} + 1 B_{3g} + 1 A_u + 1 B_{1u} + 2 B_{2u} + 2 B_{3u}) internal Si-O stretching modes above 820 cm^{-1}.

The sets of vibrational peaks detected in the simultaneous high-*P* and high-*T* spectra (**Fig. 2(a-c)**) were consistent with those obtained at ambient conditions, and the vibrational signals become weaker and broader at elevated temperatures and pressures inside the DAC chambers. The fitted vibrational frequencies are listed in **Table S1** in the supporting materials. The intensities of the vibrational bands vary at elevated temperature due to the Bose-Einstein phonon population function, while we focus on the frequencies (positions of the vibrational bands) in this Raman measurement. No phase transition has been observed in these measurements up to 15 GPa and 800 K, and these modes gradually shift to higher frequencies with increasing pressure, whereas to lower frequencies at elevated temperatures. The most intensive Si-O stretching modes in the frequency ranges of 812 – 828 cm^{-1} and 835 – 860 cm^{-1} were always detected as the characteristic peaks for olivine.

The vibrational frequencies (v_i) are generally believed to be in negative linear dependence with the volume (V) in isotropic approximation (e.g., Hofmeister and Mao 2002;

Stacey and Hodgkinson 2019). Based on a recently proposed Mie-Grüneisen-Debye (MGD) thermal EOS in the 3rd-order Birch-Murnaghan form for olivine with the mantle composition (Angel et al. 2018), we can approximate the volume as a function of P (GPa) and T (K) as: $V/V_0 = 1 + 3.8(2)\cdot10^{-5}\cdot (T\text{-}300) - 6.5(3)\cdot10^{-3}\cdot P - 1.3(1)\cdot10^{-6}\cdot(T\text{-}300)\cdot P$ in the P-T range of $0 < P < 14$ GPa and $300 < T < 1800$ K (V_0 is the ambient volume), which will be illustrated more in the following discussion and **Fig. 4(d)**. The fitting residual for V/V_0 is within $\pm1.8\times10^{-3}$ with $R^2 = 0.996$. Hence, we fit $v_i(T,P)$ to Eqn (1) for the combination of the datasets from Liu et al. (2021) and this study, which is in a similar functional form as V/V_0 above:

$$v_i(T,P) = v_0 + a\cdot(T-300) + b\cdot P + k\cdot(T-300)\cdot P \qquad (1)$$

where v_0 is the vibrational frequency at ambient conditions, and the variables of T and P are in the units of K and GPa, respectively. The fitted coefficients of a, b and k are listed in **Table 1** for each of the Raman-active modes. The a (cm^{-1}/K) and b (cm^{-1}/GPa) coefficients from this fitting are generally consistent with the T- and P-derivatives of v_i's from Liu et al. (2021), whereas the coefficient k for the third term on the right side of Eqn. (1) (i.e., the cross term for both P and T) is typically in a magnitude no more than 1.1×10^{-3} cm^{-1}/(GPa·K).

It is noted that a systematical deviation up to 5 cm^{-1} would be caused from the current fitting results for v_i's at 800 K and high pressures, if this cross item was ignored due to a lack of simultaneous high-P,T dataset. In order to further illustrate the fitting results, we selected the strong Si-O stretching band around 823 cm^{-1} as an example. Variation of this mode with pressure is plotted in **Fig. 3(a)** at various temperatures, and linear regression is fitted between v_i and P at each temperature. At T = 300 K, the data points measured in NaCl (this study, solid circles) are in agreement with those measured in Ar (Liu et al. 2021, open circles). The spectra connected at simultaneous high-P,T inside DAC are also consistent with the previous high-T measurement in

This is the peer-reviewed, final accepted version for American Mineralogist, published by the Mineralogical Society of America.
The published version is subject to change. Cite as Authors (Year) Title. American Mineralogist, in press.
DOI: https://doi.org/10.2138/am-2023-9052. http://www.minsocam.org/

the heating stage at P = 0 GPa. The fitting residuals (Δv_i) are generally within ±1.5 cm^{-1} (**Fig. 3b**), which is typical for these vibrational modes. In addition, the P- and T-dependences for the other measured vibrational modes are also illustrated in supplementary **Fig. S2(a-c)**.

3.2 The mode Grüneisen and intrinsic anharmonic parameters

The shift of vibrational frequency at high-T and high-P conditions is generally viewed as combination of two contributions (e.g. Gillet et al. 1991, 1997): (1) a pure volumetric contribution due to thermal expansion and compression, which could be simply interpreted as quasi-harmonicity and (2) an intrinsic anharmonic contribution which is in positive correlation with temperature and independent with volume variation. Firstly, the isobaric (γ_{iP}) and isothermal (γ_{iT}) mode Grüneisen parameters are introduced to describe variation of the frequency (v_i) with temperature and pressure, respectively:

$$\gamma_{iP}(T,P) = \left(\frac{\partial \ln v_i}{\partial \rho}\right)_P = -\frac{1}{\alpha(T,P)} \cdot \left(\frac{\partial \ln v_i(T,P)}{\partial T}\right)_P \quad (2)$$

$$\gamma_{iT}(T,P) = \left(\frac{\partial \ln v_i}{\partial \rho}\right)_T = K_T(T,P) \cdot \left(\frac{\partial \ln v_i(T,P)}{\partial P}\right)_T \quad (3)$$

where α and K_T are the thermal expansion coefficient and isothermal bulk modulus at high-P,T conditions, respectively. Next, the intrinsic anharmonic parameter (a_i), describing variation of the frequency with T at constant volume, can be derived from the difference between γ_{iT} and γ_{iP}:

$$a_i(T,P) = \left(\frac{\partial \ln v_i}{\partial T}\right)_V = \alpha(T,P) \cdot [\gamma_{iT}(T,P) - \gamma_{iP}(T,P)] = \left(\frac{\partial \ln v_i}{\partial T}\right)_P + \alpha \cdot K_T \cdot \left(\frac{\partial \ln v_i}{\partial P}\right)_T \quad (4)$$

In this calculation, we adopt the MGD P-V-T EOS by Angel et al. (2018), which is constructed in the 3rd-order Birch-Murnaghan form: K_{T0} = 126.3(2) GPa at the ambient condition

This is the peer-reviewed, final accepted version for American Mineralogist, published by the Mineralogical Society of America.
The published version is subject to change. Cite as Authors (Year) Title. American Mineralogist, in press.
DOI: https://doi.org/10.2138/am-2023-9052. http://www.minsocam.org/

with a pressure derivative of K_0' = 4.54(6), the Debye temperature q_{D0} = 644(9) K, and the Grüneisen parameter γ_0 = 1.044(4) with a volume dependence of q = 1.9(2) as in $\gamma = \gamma_0 \cdot \left(\frac{V}{V_0}\right)^q$. The isothermal bulk modulus and thermal expansion coefficient are calculated as a function of temperature (300 < T < 1800 K), at the selected pressures of 0, 3, 6, 9, 12 and 14 GPa (**Fig. 4a,b** and **Table S2** in the supporting materials). The K_T modulus decreases at elevated temperature, and increases with increasing pressure, whereas positive T-dependence and negative P-dependence are observed for α. The calculated $\alpha(T)$ profile at P = 0 GPa is consistent with that for $Fo_{87}Fa_{13}$ olivine (Kroll et al. 2012), with discrepancy typically within ±5 %. The product of $\alpha \cdot K_T$ (**Fig. 4c**) increases rapidly below 700 K while smoothly at higher temperature, and its magnitude decreases by 9.7 % from 0 to 14 GPa, at T = 1800 K. Finally, the volume at high-P,T conditions (**Fig. 4d**) is derived according to the definition of the thermal expansion coefficient:

$$V(T,P) = V(300K,P) \cdot exp[\int_{300K}^{T} \alpha(T,P) \cdot dT] \quad (5)$$

which is also listed in **Table S2** and will be utilized in the following calculations. Besides, the Anderson-Grüneisen parameter (δ_T) is also extensively adopted to describe the isobaric variation of K_T with volume, as defined in Eqn (6) (e.g., Anderson 1995; Angel et al. 2018):

$$\delta_T = -\frac{1}{\alpha \cdot K_T}\left(\frac{\partial K_T}{\partial T}\right)_P = -\left(\frac{\partial \ln K_T}{\partial lnV}\right)_P \quad (6)$$

The computed $\delta_T(P,T)$ for olivine is also plotted in **Fig. 4(e)**, which exhibits negative T-dependence, since the product of $\alpha \cdot K_T$ increases at elevated temperature for a constant pressure.

Based on the calculated K_T and α at high-P,T conditions, we computed the $\gamma_{iT}(T,P)$ (Eqn 2) and $\gamma_{iP}(T,P)$ (Eqn 3) parameters for the vibrations **(Fig. 5a,b** for a representative example of

the mode at 823 cm^{-1}). The isothermal and isobaric Grüneisen parameters are distributed in the value ranges of 0.54 – 1.5 and 0.35 – 0.66, respectively, both of which exhibit negative *T*- and positive *P*-dependences. The anharmonic parameter a_i (10^{-5} K^{-1}) is systematically in negative values (**Fig. 5c**), and its magnitude decreases from 1.26 - 1.33 at T = 300 K to 0.92 – 1.02 at 1800 K. It should be noted that all the 1σ uncertainties from measurements, including temperature (~ 1 K), pressure (< 0.3 GPa) and frequency fitting (< 1.5 cm^{-1}), would be propagated in the following calculation for thermodynamic properties (Grüneisen and anharmonic mode parameters, heat capacities, thermodynamic Grüneisen parameters γ, bulk modulus K_S and velocity V_Φ, as well as adiabatic *T*-*P* profile), which are also included in supplementary **Table S2**.

On the other hand, Hofmeister and Mao (2002) pointed out that for some particular vibrations, such as internal Si-O stretching modes and transition of MO_6, it is appropriate to utilize the polyhedral bulk moduli (K_X) to calculate the isothermal mode Grüneisen parameters (Eqn. 3) in the polyatomic structures. They adopted the moduli of 147 GPa for MgO_6 and 423 GPa for SiO_4 in Mg_2SiO_4-spinel (Hazen and Yang 1999), to calculate the γ_{iT} parameters for structure-related forsterite. A following high-*T* structure refinement on Mg-pure ringwoodite gave the averaged polyhedral thermal expansion coefficients (α_X) of $2.6(4)\times10^{-5}$ K^{-1} for MgO_6 while $0.9(3)\times10^{-5}$ K^{-1} for SiO_4 (Ye et al. 2012). Consequently, the product of $\alpha_X \cdot K_X$ is about 3.8(6) MPa/K for both MgO_6 and SiO_4, which is also very close to that for the bulk (**Fig. 4c**) from *P*-*V*-*T* EOS fitting (Angel et al. 2018). It may cause some discrepancies when we routinely compute the mode Grüneisen parameters of γ_{iT} and γ_{iP} with only bulk α and K_T, but the impact on the anharmonic mode parameter (a_i) should be insignificant. It is therefore that the a_i parameters, rather than γ_{iT} or γ_{iP}, will be utilized in the following calculation for the anharmonic

This is the peer-reviewed, final accepted version for American Mineralogist, published by the Mineralogical Society of America.
The published version is subject to change. Cite as Authors (Year) Title. American Mineralogist, in press.
DOI: https://doi.org/10.2138/am-2023-9052. http://www.minsocam.org/

292 contribution to the thermodynamic properties.

293

294 **3.3 Anharmonic contribution to heat capacities**

295 According to Kieffer's model for the vibrational contribution to the isochoric heat
296 capacities C_V in poly-atomic minerals (Kieffer 1979, 1980), the optical modes, including both
297 Raman-active and IR-active ones, can be divided into several continua based on their
298 attributions. For the case of forsterite, a model of density of states (DOSs) has been adopted to
299 calculate the heat capacity (e.g. Gillet et al. 1991) as: (1) 52 modes in continuum I from 105 to
300 482 cm^{-1}, including 45 lattice vibrations and 7 symmetric O-Si-O bending ones (v_2); (2) 13
301 modes in continuum II in the range of 505 - 644 cm^{-1}, including 12 asymmetric O-Si-O bending
302 vibrations (v_4) and 1 v_2; (3) 16 Si-O stretching (v_1 and v_3) modes in continuum III from 825 to
303 975 cm^{-1}. It is widely known that the vibrational frequencies systematically shift to lower
304 frequencies with substitution of Mg^{2+} by Fe^{2+} in olivine (e.g. Breitenfeld et al. 2018), and the
305 upper (v_{ui}) and lower (v_{li}) limits of each continuum in San Carlos olivine have been modified as:
306 103 – 478, 499 – 639 and 822 – 973 cm^{-1} for continua I, II and III, respectively (Liu et al. 2021).
307 Then, the capacity of C_V (J/(mol·K)) in harmonic approximation can be derived as below:

308 $$C_V(T) = \left(\frac{\partial U}{\partial T}\right)_V = 3 \cdot n \cdot R \sum_{i=1}^{3} \frac{n_i}{N} \int_{x_{li}}^{x_{ui}} \frac{{x_i}^2 \exp(x_i) dx_i}{(x_{ui}-x_{li})[\exp(x_i)-1]^2} = 3 \cdot \frac{n}{N} \cdot R \sum_{i=1}^{3} C_{vi}^{h}(T) \quad (7)$$

309 where n (7) and N (84) are the numbers of atoms per formula and vibrational modes per unit cell,
310 respectively. R is the gas constant and C_{vi}^{h} is the microscopic heat capacity from each continuum
311 in harmonic approximation. The dimensionless frequency is defined as $x_i = h \cdot c \cdot v_i/(k_B \cdot T)$, where h,
312 c and k_B are the Planck, light speed in vacuum, and Boltzmann constants, individually.

This is the peer-reviewed, final accepted version for American Mineralogist, published by the Mineralogical Society of America.
The published version is subject to change. Cite as Authors (Year) Title. American Mineralogist, in press.
DOI: https://doi.org/10.2138/am-2023-9052. http://www.minsocam.org/

On the other hand, the intrinsic anharmonic contribution becomes essential and necessary for accurate determination of thermodynamic properties, especially at high temperatures (Gillet et al. 1991; Polyakov 1998; Dorogokupets and Oganov 2004; Wu 2015). Since the a_i parameters have already been determined as a function of both temperature and pressure in the above section, we propose a new approach to compute the anharmonic contribution to the heat capacity C_V at high temperatures, which is similar to that from Gillet et al. (1991):

$$C_V(T,P) = 3 \cdot \frac{n}{N} \cdot R \sum_{i=1}^{3} C_{vi}^{h}(T,P) \cdot (1 - 2 \int_0^T a_i(T,P) \cdot dT) \quad (8)$$

Following the above computation procedure for the example of 823 cm^{-1}, we calculated the averaged anharmonic parameters for the modes in Continua I, II and III (**Fig. 6(a-c)**). The magnitudes of the a_i parameters systematically increase with increasing pressure, indicating that the intrinsic contribution to thermodynamics would become higher at elevated pressure. The a_i parameters for the internal vibrations inside the rigid units of SiO_4 are typically in smaller magnitudes, as compared those for the rotations or translations of these units (Liu et al. 2019b). When $T \rightarrow 0$ K, the thermal expansion coefficient decreases to zero, and consequently, the a_i parameters also approach 0 according to Eqn (4). In order to have a precise evaluation of the anharmonic contribution to thermodynamics, the $a_i(T)$ curves are fitted in 6^{th}-order polynomials for temperature ($R^2 \geq 0.99$), and the corresponding coefficients (c_i, i = 1, 2...6, with c_0 fixed at 0) are listed in **Table S3** in the supporting materials.

The vibrational modes generally shift to higher frequencies at elevated pressure, as supported by both high-pressure Raman (e.g. Gillet et al. 1991; Liu et al. 2021; this study) and infrared (e.g. Hofmeister et al. 1989; Wang et al. 1993; Hofmeister 1997) spectra on olivine-group minerals. The P-dependences of v_i's (dv_i/dP, $cm^{-1} \cdot GPa^{-1}$) from these studies are compared in **Fig. 7**, and there are no clearly systematical differences for the slopes between the Raman and

This is the peer-reviewed, final accepted version for American Mineralogist, published by the Mineralogical Society of America.
The published version is subject to change. Cite as Authors (Year) Title. American Mineralogist, in press.
DOI: https://doi.org/10.2138/am-2023-9052. http://www.minsocam.org/

infrared measurements. To simplify calculation, we adopt the averaged rates of 3.2(4), 2.3(3) and 3.2(7) cm^{-1}/GPa for the measured modes in continua I, II and III, respectively. Correspondingly, high-pressure $C_V(T)$ profiles in Kieffer's model are computed according to the pressure effect on the vibrational frequencies. The harmonic $C_V(T)$ at selected pressures is illustrated in **Fig. 8a** and listed in **Table S2**. The value of C_V(0 GPa) is 5 % higher than that for C_V(14 GPa) at 300 K, while this difference decreases to less than 0.2 % at 1800 K (**Fig. 8b**).

The correlation between the isochoric and isobaric (C_P) heat capacities is expressed below:

$$C_P(T,P) = C_V(T,P) + T \cdot V \cdot \alpha(T,P)^2 \cdot K_T(T,P) \quad (9)$$

where V is the molar volume (in the unit of m^3/mol). According to the calculated variables of α, K_T and V at high-T,P conditions above, we also compute the $C_P(T,P)$ profiles (**Fig. 8c**). Similarly, the isobaric heat capacity also decreases at elevated pressure, and the C_P difference between 0 and 14 GPa is as large as about 5 % at T = 1800 K (**Fig. 8d**), since both the volume and thermal expansion coefficient decrease at elevated pressure.

The anharmonic contribution to the heat capacities ($\Delta C = C_{anh} - C_{har}$) is plotted at various P-T conditions in **Fig. 8(e)**, which is consistently positive since the a_i parameters are in negative values. At T = 1800 K and P = 0 GPa, the anharmonic contribution is equal to 7.9 $J \cdot mol^{-1} \cdot K^{-1}$, which is 22 % smaller than the previous calculation (Liu et al. 2021). In the previous model, the a_i parameters were treated as constants, independent of temperature. However, this study reveals that the a_i parameters decrease at elevated temperature. Meanwhile, even at the high temperature of 1800 K, ΔC(14 GPa) is only 1.6 $J \cdot mol^{-1} \cdot K^{-1}$ higher than ΔC(0 GPa), which accounts for less than 1 % of the magnitude of C_V(1800 K) (**Fig. 8f**). Hence, the variation of C_P at high pressure

358 mostly comes from the pure volumetric variation with pressure (i.e. *P*-*V*-*T* EOS), instead of the
359 variation of vibrational frequencies. In order to check the validation of anharmonic contribution,
360 the modeled $C_P(T)$ is compared with the high-*T* measurements on the end-members of forsterite
361 and fayalite at *P* = 0 GPa (**Fig. 9**) (Gillet et al. 1991; Saxena et al. 1993; Benisek et al. 2012).
362 Fe^{2+} incorporation seems to increase the isobaric heat capacity as implied by the comparison
363 between Mg_2SiO_4 and Fe_2SiO_4. The harmonic C_P profile for $Fo_{89}Fa_{11}$ located even below those
364 for Fo_{100}, while the anharmonic correction provides a more reasonable model between forsterite
365 and fayalite.

366 This simultaneous high-*P,T* Raman measurement indicates that the pressure effect on the
367 intrinsic anharmonicity is much smaller, as compared with that on the external anharmonicity
368 (thermal expansivity). When the pressure was increased from 0 to 14 GPa, the thermal expansion
369 coefficient, $\alpha(T)$, was decreased by 40 (at 300 K) – 48 (at 1800 K) % (**Fig. 4b**). In conclusion,
370 the intrinsic anharmonic contribution is still important for the thermodynamic properties at high
371 temperatures and ambient pressure. When extrapolated to simultaneously high-*P*,*T* conditions, it
372 is reasonable to just consider the pure volumetric contribution (from *P*-*V*-*T* EOS) for the pressure
373 effect, and the consequent uncertainty should be within 1 % for the cases of the heat capacities as
374 discussed above.

375

376 **3.4. Thermodynamic Grüneisen parameters and bulk seismic velocities**

377 Based on the derived thermal expansion coefficient, isothermal bulk modulus and
378 isochoric heat capacity at high *P*-*T* conditions in the above sections, we can also derive the
379 thermodynamic Grüneisen parameter (γ) (e.g. Liebfried and Ludwig 1961; Anderson et al. 1991)

This is the peer-reviewed, final accepted version for American Mineralogist, published by the Mineralogical Society of America.
The published version is subject to change. Cite as Authors (Year) Title. American Mineralogist, in press.
DOI: https://doi.org/10.2138/am-2023-9052. http://www.minsocam.org/

as below:

$$\gamma(T,P) = \left(\frac{\partial P}{\partial U}\right)_V \cdot V = \frac{\alpha(T,P)\cdot K_T(T,P)\cdot V(T,P)}{C_V(T,P)} \quad (10)$$

It is noted that this γ parameter is different from the isothermal and isobaric mode Grüneisen parameters above. The former ones refer to variation of local vibrational modes with pressure and temperature, while this thermodynamic γ parameter can be used to relate the bulk thermal energy to the thermal pressure based on MGD *P*-*V*-*T* equation. In this study, the connection of mode and thermodynamic Grüneisen parameters is fulfilled by the intrinsic anharmonic contribution (the a_i parameters in Eqns 4 and 8) to the heat capacity C_V. The $\gamma(T,P)$ parameters are computed in both harmonic and anharmonic models (**Fig. 10(a,b)**), which are fitted as 3rd-polynomial functions of *T*, and the coefficient for each item is fitted as a linear function of *P* with $R^2 \geq 0.98$:

$$\gamma_{har}(T,P) = (0.001 \cdot P - 0.128) \cdot x^3 + (-0.003 \cdot P + 0.531) \cdot x^2 + (0.002 \cdot P - 0.646) \cdot x - 0.013 \cdot P + 1.351 \quad (11)$$

$$\gamma_{anh}(T,P) = (0.001 \cdot P - 0.130) \cdot x^3 + (-0.003 \cdot P + 0.523) \cdot x^2 + (0.003 \cdot P - 0.677) \cdot x - 0.013 \cdot P + 1.349 \quad (12)$$

where the fractional temperature $x = T/1000$.

At a given temperature *T*, the thermodynamic Grüneisen parameter systematically decreases at elevated pressure, due to compression of the volume. In addition, the γ parameters decrease significantly from 300 to 700 K due to rapidly increasing C_V. Above 900 K, γ_{har} increases smoothly by nearly 5 % up to T = 1800 K, whereas γ_{anh} remains almost constant. The anharmonic γ parameter is smaller than the harmonic one, since the intrinsic anharmonicity has

This is the peer-reviewed, final accepted version for American Mineralogist, published by the Mineralogical Society of America.
The published version is subject to change. Cite as Authors (Year) Title. American Mineralogist, in press.
DOI: https://doi.org/10.2138/am-2023-9052. http://www.minsocam.org/

399 positive contribution to C_V, and the difference is about 1 % at T = 300 K, which increases to 8 –
400 9 % at 1800 K. Besides, both the γ_{har} and γ_{anh} parameters at the selected pressures are plotted as a
401 function of normalized volume (V/V_0) (**Fig. 10c**), where V_0 is the volume at the ambient
402 condition.

403 These high-T Grüneisen parameters (above 800 K) in both harmonic and anharmonic
404 models agree with those fitted from the recent MGD *P-V-T* EOSs for olivines (e.g.,
405 Dorogokupets et al. 2015; Angel et al. 2018; Katsura 2022), whereas Liu and Li (2006)
406 predicted a much higher $\gamma(V)$ parameter. In addition, our modeled γ_0 at the ambient condition is
407 4 % smaller than that from Isaak (1992). It is noted that in a typical MGD *P-V-T* EOS fitting
408 approach, the heat capacity and thermal free energy are approximated by the harmonic Debye
409 model, which basically considers the contributions from the three acoustic modes (one
410 longitudinal and two transverse), and ignores the optical vibrations at higher frequencies. In the
411 case of olivine with 28 atoms (4 formula units) in its unit cell, there are totally 81 optical modes
412 together with 3 acoustic ones, and the contribution from the optical vibrations should also be
413 considered for accurate calculation of the thermodynamic properties. Strictly speaking, the
414 thermodynamic Grüneisen parameter cannot be simply described as a function of volume for
415 silicate minerals with multiple atoms, and two variables out of P, V, T are needed, like $\gamma(P,T)$,
416 $\gamma(V,T)$ or $\gamma(V,P)$.

417 The relationship between adiabatic (K_S) and isothermal (K_T) bulk moduli is expressed
418 below:

419 $$K_S(T,P) = K_T(T,P) \cdot (1 + \alpha(T,P) \cdot \gamma(T,P) \cdot T) \quad (13)$$

420 Based on the calculated K_T, the thermal expansion coefficient α, and the thermodynamic

This is the peer-reviewed, final accepted version for American Mineralogist, published by the Mineralogical Society of America.
The published version is subject to change. Cite as Authors (Year) Title. American Mineralogist, in press.
DOI: https://doi.org/10.2138/am-2023-9052. http://www.minsocam.org/

421 Grüneisen parameters at simultaneously high-*P,T* conditions, we can derive $K_S(T,P)$ in both the
422 harmonic and anharmonic models (**Fig. 11a**). The anharmonic contribution is marginal to K_S,
423 which only causes a reduction of 0.6 – 0.7 GPa even at the high temperature of 1800 K. Our
424 model yields K_{S0} = 127.5(1) GPa with a *T*-derivative of $(\partial K_S/\partial T)_P$ = -0.018(1) GPa/K and a *P*-
425 derivative of K_S' = 4.32(5). Next, the bulk sound velocity (V_Φ, km/s) can be further calculated
426 based on the derived K_S and density ρ (**Fig. 11b**):

427 $$V_\Phi(T,P) = \sqrt{\frac{K_S(T,P)}{\rho(T,P)}} \quad (14)$$

428 The difference between harmonic and anharmonic velocities is also tiny, which is still within
429 0.02 Km/s even at T = 1800 K. The anharmonic velocity is fitted as a function of T (K) and P
430 (GPa) as: $V_\Phi(T,P) = 6.22(2) + 0.069(3)\times P - [3.74(15) - 0.075(13)\cdot P]\cdot 10^{-4}\times(T\text{-}300)$. On the other
431 hand, Liu et al. (2005) directly measured the seismic velocities of V_P and V_S on San Carlos
432 olivine up to 8 GPa and 1073 K, and the bulk sound velocity can also be computed according to
433 the relationship of $V_\Phi^2 = V_P^2 - 4/3\cdot V_S^2$. An agreement is met between both these studies with a
434 discrepancy approximately 1 %, which is comparable to the uncertainty of measurement.

435

436 **3.5. Adiabatic temperature profile of olivine**

437 The thermodynamic Grüneisen parameter can be adopted to calculate the adiabatic
438 temperature profile in the mantle as following (Ramakrishnan et al. 1978; Boehler et al. 1979;
439 Brown and Shankland 1981; Katsura 2022):

440 $$\gamma(P,T) = -\left(\frac{\partial ln T_S}{\partial ln V}\right)_S = \frac{K_S(P,T)}{T_S}\cdot\frac{dT_S}{dP} \quad (15)$$

441 where the subscript *S* stands for an adiabatic process (with constant entropy). We further

This is the peer-reviewed, final accepted version for American Mineralogist, published by the Mineralogical Society of America.
The published version is subject to change. Cite as Authors (Year) Title. American Mineralogist, in press.
DOI: https://doi.org/10.2138/am-2023-9052. http://www.minsocam.org/

compute the adiabatic temperature, T_S, profiles in both the harmonic and anharmonic models (**Fig. 12**), which can be approximated as a linear function of pressure ($0 \leq P \leq 14$ GPa) with $R^2 \geq 0.997$:

$$T_S^{har}(P) = [0.0089(1) \cdot T_0 - 1.028(6)] \cdot P + T_0 \quad (16)$$

$$T_S^{anh}(P) = [0.0078(1) \cdot T_0 - 0.487(5)] \cdot P + T_0 \quad (17)$$

where T_0 is the 'starting' temperature anchored at P = 0 GPa (i.e. T_S(0 GPa)). The anharmonic thermal gradient of dT_S/dP (K/GPa) is slightly smaller than that in the harmonic approximation (**Table S4** in the supplementary materials), since the anharmonic correction has negative contribution to the γ parameter. The T_S profile with T_0 = 1600 K matches a recently proposed adiabatic geotherm in the upper mantle by Katsura (2022), which is a revision for the previous one (Katsura et al. 2010) based on the updated *P-V-T* EOSs and phase diagram, as well as *P*-correction for the thermocouple in multi-anvil press. The corresponding slope of dT_S/dP is 13.40(16) and 12.35(16) K/GPa for the harmonic and anharmonic models, respectively, and the reported value is 12.04(4) K/GPa (Katsura 2022).As suggested by Eqns (16) and (17), the pressure gradient of the adiabatic T_S profile is independent of pressure, and in positive dependence with the starting temperature T_0, which increases from 2.21 (at T_0 = 300 K) to 14.05 K/GPa (at 2000 K) with the anharmonic correction.

4 Implications for thermodynamic properties in the Earth and planetary mantles

Previous vibrational spectra on olivine were obtained at high-*T* or high-*P* conditions, and the derived anharmonic parameters (a_i) were constants, independent with temperature or pressure. We conducted simultaneous high-*P,T* Raman measurements, and modeled the a_i

parameters as a function of both temperature and pressure. One of the major findings from this study is that the anharmonic contributions to the thermodynamic properties, like heat capacities, could be overestimated if the a_i parameters were treated as constants like before. Pressure has significant impact on the external anharmonicity (thermal expansivity), while a marginal effect on the intrinsic anharmonicity. Hence, when modeling the thermodynamic properties of minerals at high-P,T conditions in the Earth and planetary interiors, it is still important to conduct the anharmonic correction at high temperatures, and the pressure effect could be simply attributed to variation of volume based on P-V-T EOSs. The anharmonic contribution can be ignored for the high-T bulk moduli of K_T and K_S.

The thermodynamic Grüneisen parameter of olivine, $\gamma(P,T)$, is precisely determined based on combination of isothermal compression (for P-V-T EOS) and vibrational spectroscopy (for heat capacity). Noted that temperatures could not be directly measured in early shockwave experiments, but were inferred according to the Grüneisen parameters from P-V-T EOSs (e.g., Ahrens et al. 1971; Jackson and Ahrens 1979; Syono et al. 1981; Mosenfelder et al. 2007). At present, new technology has been introduced for measuring shock temperatures based on the gray-body Planck spectra (e.g., Ozaki et al. 2009; Sekine et al. 2016), but only very high temperatures (well above 3000 K) could be accurately determined. Hence, reliable γ parameter is still key for constraining shock temperatures especially in the T-ranges relevant to the Earth and many planetary mantles.

This calculation for the Grüneisen parameter further provides an example for constraining the radial (adiabatic) temperature distributions, which is useful in various geodynamic settings inside Earth's and planetary mantles where convection is active. In the mantle of a terrestrial planet, the pressure increases more quickly with increasing depth (i.e.

larger dP/dz, where z is the depth in the mantle), if the radius (gravity) is greater. Then, the gradient of the geotherm (dT_S/dz in K/km) would be consequently larger in the adiabatic compression. In this case, we can expect that dT_S/dz in the Earth's mantle is larger than those in the early lunar and Martian mantles (e.g. Ziethe et al. 2009; Šrámek and Zhong 2010), when their mantle convections were active and volcanism was widespread on their planetary surfaces. In addition, temperature is also the main factor of controlling the depth of the 410-km discontinuity, which is caused by olivine-wadsleyite phase transition (e.g. Katsura et al. 2004). Precise adiabatic T-gradient is also important for constraining variations of the 410-km discontinuity under various geodynamic settings.

The heat capacities of olivine at high-P,T conditions, C_P and C_V, are also fundamental for constraining the thermal transport properties in the Earth's and planetary interiors (e.g. Dubuffet et al. 1999; Tosi et al. 2013). The correlation between thermal conductivity (λ) and thermal diffusivity (κ) is expressed as: $\lambda(P,T) = C(P,T) \times \rho(P,T) \times \kappa(P,T)$ (Zhang et al. 2019; 2023), where the density $\rho(P,T)$ can be computed from P-V-T EOS, while the heat capacity C is taken as average of C_V and C_P. Our modeled heat capacities for San Carlos olivine are $C_{V,\mathrm{har}}$ = 807.7 J/kg/K and $C_{P,\mathrm{har}}$ = 815.4 J/kg/K with anharmonic contribution of ΔC = 7.9 J/kg/K at the ambient condition, which is consistent with that for Fo_{90} olivine (815 J/kg/K) extrapolated from the measurements on $\lambda(P,T)$ and $\kappa(P,T)$ (Zhang et al. 2019). Meanwhile, the high-P vibrational spectroscopic measurements give the P-derivates of isobaric heat capacity (dC_P/dP, in the unit of J/kg/K/GPa) for olivine increases from -3.14 at 300 K to -1.94 at 700 K, and then decrease gradually to -5.03 at 1800 K, which is comparable to those from the simultaneous high-P measurements on thermal conductivities and diffusivities (Osako et al. 2004; Zhang et al. 2019). Hence, the datasets from different experiments could be combined together to have more precise

constraint on the heat transport properties of minerals at high-*P,T* conditions, which are important for mantle convection, subduction dynamics, as well as cooling histories of rocky planets.

Acknowledgments

This project was supported by the National Natural Science Foundation of China (42072050), the National Key Research and Development Program of China (Grant No. 2018YFA0702700), the Science Fund for Distinguished Young Scholars of Hubei Province (2020CFA104), as well as the "CUG Scholar" Scientific Research Funds at China University of Geosciences (Wuhan) (Project No. 2022117). Dan Liu is funded by China Scholarship Council. Many thanks to Dr. Yao Wu for supporting the sample.

Reference

Agee, C.B. (1998) Phase transformations and seismic structure in the upper mantle and transition zone. In R.J. Hemley Ed., Ultrahigh-Pressure Mienralogy: Physics and Chemistry of Earth's Deep Interior, Reviews in Mineralogy and Geochemistry, 37, p. 165-200. Mineralogical Society of America, Washington, DC.

Ahrens, T.J., Lower, J.H., and Lagus, P.L. (1971) Equation of State of Forsterite. Equation of State of Forsterite. Journal of Geophysical Research, 76, 518-528.

Anderson, D.L. (1995) Equations of State of Solids for Geophysics and Ceramic Science, 432p. Oxford University Press, Oxford, U.K.

Anderson, D.L. (2007) New theory of the Earth, 384p.Cambridge University Press, Cambridge.

Anderson, O.L., Isaak, D.L., and Oda, H. (1991) Thermoelastic parameters for six minerals at high-temperature. Journal of Geophysical Research: Solid Earth, 96, 18037-18046.

Angel, R.J., Alvaro, M., and Nestola, F. (2018) 40years of mineral elasticity: a critical review and a new parameterisation of equations of state for mantle olivines and diamond inclusions. Physics and Chemistry of Minerals, 45, 95-113.

Benisek, A., Kroll, H., and Dachs, E. (2012) The heat capacity of fayalite at high temperatures. American Mineralogist, 97, 657-660.

Boehler, R., Skoropanev, A., O'Mara, D., and Kennedy, G.C. (1979) Grüneisen parameter of quartz, quartzite and fluorite at high pressures. Journal of Geophysical Research: Solid Earth, 84, 3527-3531.

Breitenfeld, L.B., Dyar, M.D., Carey, C.J., Tague, Jr., T.J., Wang, P., Mullen, T., and Parente, M. (2018) Predicting olivine composition using Raman spectroscopy through band shift and multivariate analyses. American Mineralogist, 103, 1827-1836.

Brown, J.M., and McQueen, R.G. (1986) Phase transitions, Grüneisen parameter, and elasticity for shocked iron between 77 GPa and 400 GPa. Journal of Geophysical Research: Solid Earth, 91(B7), 7485-7494.

Brown, J.M., and Shankland, T.J. (1981) Thermodynamic parameters in the Earth as determined from seismic profiles. Geophysical Journal International, 66, 579-596.

Burns, R.G., and Huggins, F.E. (1972) Cation determinative curves for Mg-Fe-Mn olivines from vibrational spectra. American Mineralogist, 57, 967-985.

Chopelas, A. (1990) Thermal properties of forsterite at mantle pressures derived from vibrational spectroscopy. Physics and Chemistry of Minerals, 17, 149-156.

553 Chopelas, A. (1991) Single crystal Raman spectra of forsterite, fayalite, and monticellite.
554 American Mineralogist, 76, 1101–1109.

555 Cynn, H., Hofmeister, A.M., Burnley, P.C., and Navrotsky, A. (1996a) Thermodynamic
556 properties and hydrogen speciation from vibrational spectra of dense hydrous magnesium
557 silicates. Physics and Chemistry of Minerals, 23, 361-376.

558 Cynn, H., Carnes, J.D., and Anderson, O.L. (1996b) Thermal properties of forsterite, including
559 C*v*, calculated from α K_T through the entropy. Journal of Physics and Chemistry of Solids,
560 57, 1593-1599.

561 Datchi, F., and Canny, B. (2004) Raman spectrum of cubic boron nitride at high pressure and
562 temperature. Physical Review B, 69(14), 144106.

563 Dorogokupets, P.I., and Oganov, A.R. (2004) Intrinsic anharmoncity in equations of state of
564 solids and minerals. Doklady Earth Sciences, 395, 238-241.

565 Dorfman, S.M., Jiang, F., Mao, Z., Kubo, A., Meng, Y., Prakapenka, V.B., and Duffy, T.S.
566 (2010) Phase transitions and equations of state of alkaline earth fluorides CaF_2, SrF_2, and
567 BaF_2 to Mbar pressures. Physical Review B, 78, 104102.

568 Dorfman, S.M., Prakapenka, V.B., Meng, Y., and Duffy, T.S. (2012) Intercomparison of
569 pressure standards (Au, Pt, Mo, MgO, NaCl and Ne) to 2.5 Mbar. Journal of Geophysical
570 Research, 117, B08210.

571 Dorogokupets, P.I., Dymshits, A.M., Sokolova, T.S., Danilov, B.S., and Litasov K.D. (2015) The
572 equations of state of forsterite, wadsleyite, ringwoodite, akimotoite, $MgSiO_3$-perovskite,
573 and postperovskite and phase diagram for the Mg_2SiO_4 system at pressures of up to 130GPa.
574 Russian Geology and Geophysics, 56(1-2), 172-189.

575 Dubuffet, F., Yuen, D.A., and Rabinovics, M. (1999) Effects of a realistic mantle thermal
576 conductivity on the pattern of 3D convection. Earth and Planetary Science Letters, 171,
577 401-409.

578 Farmer, V.C., and Lazarev, A.N. (1974) Symmetry and crystal vibrations. In V.C. Farmer Ed.,
579 The infrared spectra of minerals, 4, p. 51-68. Mineralogical Society of Great Britain and
580 Ireland, London.

581 Fateley, W.G., McDevitt, N.T., and Bentley, F.F. (1971) Infrared and Raman selection rules for
582 lattice vibrations: The correlation method. Applied Spectroscopy, 25, 155-173.

583 Gillet, P., Daniel, I., and Guyot, F. (1997) Anharmonic properties of Mg_2SiO_4-forsterite
584 measured from the volume dependence of the Raman spectrum. European Journal of
585 Mineralogy, 9, 255-262.

586 Gillet, P., Richet, P., Guyot, F., and Fiquet, G. (1991) High-temperature thermodynamic
587 properties of forsterite. Journal of Geophysical Research: Solid Earth, 96, 11805-11816.

588 Gillet, P., Fiquet, G., Malézieus, J.M., and Geiger, C.A. (1992) High-pressure and high-
589 temperature Raman spectroscopy of end-member garnets: pyrope, grossular and andradite.
590 European Journal of Mineralogy, 4, 651-664.

591 Guyot, F., Boyer, H., Madon, M., Velde, B., and Poirier, J.P. (1986) Comparison of the Raman
592 microprobe spectra of $(Mg,Fe)_2SiO_4$ and Mg_2GeO_4 with olivine and spinel structure.
593 Physics and Chemistry of Minerals, 13, 91-95.

594 Guyot, F., Wang, Y., Gillet, P., and Ricard, Y. (1996) Quasi-harmonic computations of
595 thermodynamic parameters of olivines at high-pressure and high-temperature: a comparison
596 with experiment data. Physics of the Earth and Planetary Interiors, 98, 17-29.

Hazen, R.M., and Yang, H. (1999) Effects of cation substitution and order-disorder on P-V-T equations of state of cubic spinels. American Mineralogist, 84, 1956-1960.

Hofmeister, A.M. (1987) Single-crystal absorption and reflection infrared spectroscopy of forsterite and fayalite. Physics and Chemistry of Minerals, 14, 499-513.

Hofmeister, A.M. (1997) Infrared reflectance spectra of fayalite, and absorption data from assorted olivines, including pressure and isotope effects. Physics and Chemistry of Minerals, 24, 535-546.

Hofmeister, A.M., and Mao, H.K. (2002) Redefinition of the mode Grüneisen parameter for polyatomic substances and thermodynamic implications. Proceedings of the National Academy of Sciences, 99, 559-564.

Hofmeister, A.M., Xu, J., Mao, H.K., Bell, P.M., and Hoering, T.C. (1989) Thermodynamics of Fe-Mg olivines at mantle pressures: Mid- and far-infrared spectroscopy at high pressure. American Mineralogist, 74, 281-306.

Holland, T.J.B., and Powell, R. (1998) An internally consistent thermodynamic data set for phases of petrological interest. Journal of Metamorphic Geology, 16, 309-343.

Huang, H., Hu, X., Jing, F., Cai, L., Shen, Q., Gong, Z., and Liu, H. (2010) Melting behavior of Fe-O-S at high pressure: A discussion on the melting depression induced by O and S. Journal of Geophysical Research: Solid Earth, 115, B05207.

Huang, H., Leng, C., Wang, Q., Yang, G., Hu, X., Wu, Y., Liu, X., and Fei, Y. (2018) Measurement of sound velocity of liquid Fe-11.8wt%S up to 211.4GPa and 6,150K. Journal of Geophysical Research: Solid Earth, 123, 4730-4739.

618 Hushur, A., Manghnani, M.H., Smyth, J.R., Nestola, F., and Frost, D.J. (2009) Crystal chemistry
619 of hydrous forsterite and its vibrational properties up to 41 GPa. American Mineralogist, 94,
620 751-760.

621 Iishi, K. (1978) Lattice dynamics of forsterite. American Mineralogist, 63, 1198-1208.

622 Isaak, D.G. (1992) High-temperature elasticity of iron-bearing olivine. Journal of Geophysical
623 Research: Solid Earth, 97, 1871-1885.

624 Ishibashi, H., Arakawa, M., Yamamoto, J., and Kagi, H. (2012) Precise determination of Mg/Fe
625 ratios applicable to terrestrial olivine samples using Raman spectroscopy. Journal of Raman
626 spectroscopy, 43, 331-337.

627 Jackson, I. and Ahrens, T.J. (1979) Shock wave compression of single-crystal forsterite. Journal
628 of Geophysical Research, 84, 3039-3048.

629 Katsura, T. (2022) A revised adiabatic temperature profile for the mantle. Journal of Geophysical
630 Research: Solid Earth, 127, e2021JB023562.

631 Katsura, T., Yamada, H., Nishikawa, O., Song, M., Kubo, A., Shinmei, T., Yokoshi, S., Aizawa,
632 Y., Yoshino, T., Walter, M.J., Ito, E., and Funakoshi, K. (2004) Olivine-wadslyeite
633 transition in the system $(Mg,Fe)_2SiO_4$. Journal of Geophysical Research: Solid Earth, 109,
634 B02209

635 Katsura, T., Yoneda, A., Yamazaki, D., Yoshino,T., and Eiji, I. (2010) Adiabatic temperature
636 profile in the mantle. Physics of the Earth and Planetary Interiors, 212-218.

637 Khan, A., Liebske, C., Rozel, A., Rivoldini, A., Nimmo, F., Connolly, J. A. D., Plesa, A.C., and
638 Giardini, D. (2018) A geophysical perspective on the bulk composition of Mars. Journal of
639 Geophysical Research: Planets, 123, 575-611.

Kieffer, S.W. (1979) Thermodynamics and lattice vibrations of minerals: 3. Lattice dynamics and an approximation for minerals with application to simple substances and framework silicates. Reviews of Geophysics, 17, 35-59.

Kieffer, S.W. (1980) Thermodynamics and lattice vibrations of minerals: 4. Application to chain and sheet silicates and orthosilicates. Reviews of Geophysics, 18, 862-886.

Kolesov, B.A., and Geiger, C.A. (2004) A Raman spectroscopic study of Fe-Mg olivines. Physics and Chemistry of Minerals, 31, 142-154.

Kolesov, B.A., and Tanskaya, J.V. (1996) Raman spectra and cation distribution in the lattice of olivines. Materials Research Bulletin, 31, 1035-1044.

Kroll, H., Kirfel, A., Heinemann, R., and Barbier, B. (2012) Volume thermal expansion and related thermophysical parameters in the Mg,Fe olivine solid-solution series. European Journal of Mineralogy, 24, 935-956.

Liebfried, G. and Ludwig, W. (1961) Theory of anharmonic effects in crystals. In F. Seitz and D. Turnbull Eds., Solid State Physics, 12, p. 275-444. Academic Press, New York.

Liu, D., Guo, X, Smyth, J. R., Wang, X., Zhu, X., Miao, Y., Bai, J., and Ye Y. (2021) High-temperature and high-pressure Raman spectra of $Fo_{89}Fa_{11}$ and $Fo_{58}Fa_{42}$ olivines: Iron effect on thermodynamic properties. Americian Mineralogist, 106, 1668-1678.

Liu, D., Pang, Y., Ye, Y., Jin, Z., Smyth, J.R., Yang, Y., Zhang, Z., and Wang, Z. (2019a) In-situ high-temperature vibrational spectra for synthetic and natural clinohumite: Implications for dense hydrous magnesium silicates in subduction zones. American Mineralogist, 104, 53-63

660 Liu, D., Wang, S., Smyth, J.R., Zhang, J., Wang, X., Zhu, X., and Ye, Y. (2019b) In situ infrared
661 spectra for hydrous forsterite up to 1243K: Hydration effect on thermodynamic properties.
662 Minerals, 9, 512.

663 Liu, L.G., and Mernagh, T.P. (1993) Raman spectra of forsterite and fayalite at high pressures
664 and room temperatures. High Pressure Research, 11, 241-256.

665 Liu, W., and Li, B. (2006) Thermal equation of state of $(Mg_{0.9}Fe_{0.1})_2SiO_4$ olivine. Physics of the
666 Earth and Planetary Interiors, 157(3-4), 188-195.

667 Liu, W., Kung, J., and Li, B. (2005) Elasticity of San Carlos olivine to 8 GPa and 1073 K.
668 Geophysical Research Letters, 32(16), L16301.

669 Manghnani, M.H., Hushur, A., Smyth, J.R., Nestola, F., Dera, P., Sekar, M., Amulele, G., and
670 Frost, D.J. (2013) Compressibility and structural stability of two variably hydrated olivine
671 samples ($Fo_{97}Fa_3$) to 34 GPa by X-ray diffraction and Raman spectroscopy. American
672 Mineralogist, 98, 1972-1979.

673 Mosenfelder, J.L., Asimow, P.D., and Ahrens, T.J. (2007) Thermodynamic properties of
674 Mg_2SiO_4 liquid at ultra-high pressures from shock measurements to 200 GPa on forsterite
675 and wadsleyite. Journal of Geophysical Research, 112, B06208.

676 Mouri, T., and Enami, M. (2008) Raman spectroscopic study of olivine-group minerals. Journal
677 of Mineralogical and Petrological Sciences, 103, 100-104.

678 Namur, O., Collinet, M., Charlier, B., Grove, T. L., Holtz, F., and McCammon, C. (2016)
679 Melting processes and mantle sources of lavas on Mercury. Earth and Planetary Science
680 Letters, 439, 117-128.

Oganov, A.R., and Dorogokupets, P.I. (2003) All-electron and pseudopotential study of MgO: equation of state, anharmonicity, and stability. Physical Review B, 67, 224110.

Oganov, A.R., and Dorogokupets, P.I. (2004) Intrinsic anharmonicity in equations of state and thermodynamics of solids. Journal of Physics: Condensed Matter, 16, 1351-1360.

Osako, M., Ito, E., and Yoneda, A. (2004) Simultaneous measurements of thermal conductivity and thermal diffusivity for garnet and olivine under high pressure. Physics of the Earth and Planetary Interiors, 143-144, 311-320.

Ozaki, N., Sano, T., Ikoma, M., Shigemori, K., Kimura, T., Miyanishi, K., Vinci, T., Ree, F.H., Azechi, H., Endo, T., Hironaka, Y., Hori, Y., Iwamoto, A., Kadono, T., Nagatomo, H., Nakai, M., Norimatsu, T., Okuchi, T., Otani, K., Sakaiya, T., Shimizu, K., Shiroshita, A., Sunahara, A., Takahashi, H., and Kodama, R. (2009) Shock Hugoniot and temperature data for polystyrene obtained with quartz standard. Physics of Plasmas, 16, 062702.

Polyakov, V.B. (1998) On anharomic and pressure corrections to the equilibrium isotopic constants for minerals. Geochimica et Cosmochimica Acta, 62, 3077-3085.

Polyakov, V.B., and Kharlashina, N.N. (1994) Effect of pressure on equilibrium isotope fractionation. Geochimica et Cosmochimica Acta, 58, 4739-4750.

Ramakrishnan, J., Boehler, R., Higgins, G.H., and Kennedy, G.C. (1978) Behavior of Grüneisen's parameter of some metals at high pressure. Journal of Geophysical Research: Solid Earth, 83, 3535-3538.

Rao, K.R., Chaplot, S.L., Chowdhury, N., Ghose, S., Hastings, J.M., Corliss, L.M., and Price, D.L. (1988) Lattice dynamics and inelastic neutron scattering from forsterite, Mg_2SiO_4:

Phonon dispersion relation, density of states, and specific heat. Physics and Chemistry of Minerals, 16, 83-97.

Richet, P., Bottinga, Y., and Javoy, M. (1977) A review of hydrogen, carbon, nitrogen, oxygen and chlorine stable isotope fractionation among gaseous molecules. Annual Review of Earth and Planetary Sciences, 5, 65-110.

Ross, N.L., and Navrotsky, A. (1987) The Mg_2GeO_4 olivine-spinel phase transition. Physics and Chemistry of Minerals, 14, 473-481.

Ross, N.L., and Navrotsky, A. (1988) Study of the $MgGeO_3$ polymorphs (orthopyroxene, clinopyroxene, and ilmenite structures) by calorimetry, spectroscopy, and phase equilibria. American mineralogist, 73, 1355-1365.

Sanchez, J. A., Reddy, V., Kelley, M. S., Cloutis, E. A., Bottke, D. N., Nesvorny, D., Lucas, M.P., Hardersen, P.S., Gaffey, M.J., Abell, P.A., and Corre, L.L. (2014) Olivine-dominated asteroids: mineralogy and origin. Icarus, 228, 288-300.

Santamaria-Perez, D., Thomason, A., Segura, A., Pellicer-Torres, J., J Manjon, F., Corà, F., McMcColl, K., Wilson, M., Dobson, D., and McMillan, P.F. (2016) Metastable structural transformations and pressure-induced amorphization in natural $(Mg,Fe)_2SiO_4$ olivine under static compression: A Raman spectroscopic study. American mineralogist, 101(7), 1642-1650.

Saxena, S.K., Chtterjee, N., Fei, Y., and Shen, G. (1993) Thermodynamic data on oxides and silicates: an assessed data set based on thermochemistry and high pressure phase equilibrium, 113 p. Springer-Verlag, Berlin Heidelberg.

Sekine, T., Ozaki, N., Miyanishi, K., Asaumi, Y., Kimura, T., Albertazzi, B., Sato, Y., Sakawa, Y., Sano, T., Sugita, S., Matsui, T., and Kodama, R. (2016) Shock compression response of forsterite. Science Advances, 2, e1600157.

Šrámek, O., and Zhong, S. (2010) Long-wavelength stagnant lid convection with hemispheric variation in lithospheric thickness: Link between Martian crustal dichotomy and Tharsis? Journal of Geophysical Research: Planets, 115, E09010.

Stacey, F.D., and Hodgkinson, J.H. (2019) Thermodynamics with the Grüneisen parameter: Fundamentals and applications to high pressure physics and geophysics. Physics of the Earth and Planetary Interiors, 286, 42-68.

Stacey, F.D., and Isaak, D.J. (2003) Anharmonicity in mineral physics: a physical interpretation. Journal of Geophysical Research: Solid Earth, 108, 2440.

Syono, Y., Goto, T., Sato, J.-I., and Takei, H. (1981) Shock compression measurements of single-crystal forsterite in the pressure range 15-93 GPa. Journal of Geophysical Research, 86, 6181-6186.

Tosi, N., Yuen, D.A., de Koker, N., and Wentzcovitch, R.M. (2013) Mantle dynamics with pressure- and temperature-dependent thermal expansivity and conductivity. Physics of the Earth and Planetary Interiors, 217, 48-58.

Uts, I., Glazyrin, K., and Lee, K.K.M. (2013) Effect of laser annealing of pressure gradients in a diamond-anvil cell using common solid pressure media. Review of Scientific Instruments, 84, 103904.

Wang, S.Y., Sharma, S.K., and Cooney, T.F. (1993) Micro-Raman and infrared spectral study of forsterite under high pressure. American Mineralogist, 78, 469-476.

745 Weidner, D.J., Wang, Y., and Vaughan, M.T. (1994) Yield strength at high pressure and
746 temperature. Geophysical Research Letters, 21(9), 753-756.

747 Wu, Z. (2015) Thermodynamic properties of wadsleyite with anharmonic effect. Earthquake
748 Science, 28, 11-16.

749 Yang, Y., Wang, Z., Smyth, J.R., Liu, J., and Xia, Q. (2015) Water effects on the anharmonic
750 properties of forsterite. American Mineralogist, 100, 2185-2190.

751 Ye, Y., Brown, D.A., and Smyth, J.R. (2012) Compressibility and thermal expansion of hydrous
752 ringwoodite with 2.5(3) wt% H_2O. American Mineralogist, 97, 573-582.

753 Zhang, Y., Yoshino, T., Yoneda, A., and Osako, M. (2019) Effect of iron content on thermal
754 conductivity of olivine with implications for cooling history of rocky planets. Earth and
755 Planetary Science Letters, 519, 109-119.

756 Zhang, Y., Yoshino, T., and Osako, M. (2023) Effect of iron content on thermal conductivity of
757 ferropericlase: Implications for planetary mantle dynamics. Geophysical Research Letters,
758 50, e2022GL101769.

759 Zhu, X., Guo, X., Smyth, J.R., Ye, Y., Wang, X., and Liu, D. (2019) High-temperature
760 vibrational spectra between $Mg(OH)_2$ and $Mg(OD)_2$: Anharmonic contribution to
761 thermodynamics and D/H fractionation for brucite. Journal of Geophysical Research: Solid
762 Earth, 124, 8267-8280.

763 Ziethe, R., Seiferlin, K., and Hiesinger, H. (2009) Duration and extent of lunar volcanism:
764 Comparison of 3D convection models to mare basalt ages. Planetary and Space Science, 57,
765 784-796.

766

767 **Figure captions:**

768

769 **Figure 1.** Pressure-temperature conditions of the Raman measurements from this study (solid
770 circles) and Liu et al. (2021) (open circles). Part of the data points from Liu et al. (2021) is
771 shown in the figure for $T \leq 800$ K and $P \leq 14$ GPa. The vertical dashed line stands for the
772 pressure at the 410-km seismic discontinuity.

773

774 **Figure 2.** Selected high-pressure Raman spectra with the backgrounds (approximated as inclined
775 lines) subtracted, which were obtained at the temperatures of **(a)** 400, **(b)** 600 and **(c)** 800 K. The
776 peak positions are labelled for the spectrum obtained at T = 400 K and P = 2.7 GPa as a
777 representative, and its signal below 700 cm^{-1} is also magnified for clarity.

778

779 **Figure 3. (a)** Pressure dependence of the vibrational mode around 823cm^{-1} at various
780 temperatures, and a linear regression (solid line) is fitted for the dataset at each temperature
781 (solid circles: this study; open circles: Liu et al., 2021). **(b)** Fitting residual for the vibrational
782 frequency and the dashed horizontal lines stand for $\Delta v_i = \pm 1.5$ cm^{-1}.

783

784 **Figure 4**. The calculated **(a)** isothermal bulk modulus K_T, **(b)** thermal expansion coefficient α, **(c)**
785 product of $K_T \cdot \alpha$, **(d)** volume variation V/V_0 and **(e)** Anderson-Grüneisen parameter as a function
786 of temperature at P = 0, 3, 6, 9, 12 and 14 GPa, based on the P-V-T EOS for mantle composition
787 olivine (Angel et al. 2018). V_0 is the unit-cell volume at the ambient condition. The black dashed

788 curve stands for the thermal expansion coefficient of $\alpha(T, 0\ \text{GPa})$ $Fo_{87}Fa_{13}$ olivine from Kroll et
789 al. (2012).

790

791 **Figure 5.** The **(a)** isothermal and **(b)** baric mode Grüneisen parameters as well as **(c)** the
792 magnitude of intrinsic anharmonic parameters ($-a_i$) for the mode around 823 cm^{-1} at various P-T
793 conditions. The 1σ uncertainties for the mode Grüneisen parameters are smaller than sizes of the
794 curves, and the statistical uncertainty for the a_i parameter is exhibited as gray area for the curve
795 at $P = 0$ GPa as a representative in **(c)**.

796

797 **Figure 6**. The averaged magnitudes for the a_i parameters in the continua of **(a)** 103 – 478 cm^{-1}
798 for translations of M^{2+} (T(M)) and SiO_4 units (T(Si)), as well as symmetric O-Si-O bending
799 modes (v_2), **(b)** 499 – 639 cm^{-1} for asymmetric O-Si-O bending modes (v_4) and one symmetric
800 O-Si-O bending mode (v_2), **(c)** 822 – 973 cm^{-1} for symmetric (v_1) and asymmetric (v_3) Si-O
801 stretching modes. The gray areas surrounding the curves at P = 0 GPa stand for the 1σ
802 uncertainty of the anharmonic parameters.

803

804 **Figure 7.** Pressure dependencies of the vibrational frequencies (dv_i/dP) for olivine-group
805 minerals from high-P Raman (solid circles for Chopelas et al. 1990; Liu et al. 2021; This study)
806 and infrared (open circles for Hofmeister et al. 1989, 1997; Wang et al. 1993) at T = 300 K.

807

808 **Figure 8.** The temperature profiles of the harmonic **(a,b)** isochoric and **(c,d)** isobaric heat
809 capacities, and **(e,f)** the anharmonic contribution ($\Delta C = C_{anh} - C_{har}$) at the selected pressures. The

pressure effect on the isochoric and isobaric heat capacities, and the anharmonic contribution are illustrated in **(b)**, **(d)** and **(f)**, respectively, in which the 1σ uncertainties are shown as gray areas for the case of P = 0 GPa. The Dulong-Petit limit for C_V at extremely high temperature is plotted as horizontal dashed line in **(a)**.

Figure 9. The modeled $C_P(T, 0\ \text{GPa})$ for San Carlos olivine in both harmonic (dashed curve) and anharmonic (solid curve), and comparison is made with the high-T measurements on the heat capacities of forsterite and fayalite (Gillet et al. 1991; Saxena et al. 1993; Benisek et al. 2012). The uncertainties for the heat capacities (< 0.25 J/K/mol) are smaller than the sizes of the curves.

Figure 10. Temperature dependence of the thermodynamic Grüneisen parameters at various pressures, in both **(a)** harmonic (dashed curves) and **(b)** anharmonic (solid curves) models. The γ parameter is also plotted as a function of normalized volume (V/V_0) in **(c)**, and compared with Those fitted in P-V-T EOSs for olivines from Isaak (1992) (γ_0 = 1.26 at the ambient condition), Angel et al. (2018) ($\gamma = 1.044(4) \times (V/V_0)^{1.9(2)}$), Liu and Li (2006) ($\gamma = 1.27(5) \times (V/V_0)^{5.64(142)}$), Katsura (2022) ($\gamma = 1.00(2) \times (V/V_0)^{2.4(5)}$), and Dorogokupet et al. (2015) ($\gamma = 1.066 \times (V/V_0)^{2.225}$). The statistical uncertainties for the Grüneisen parameters are smaller than the sizes of the curves.

Figure 11. The **(a)** adiabatic bulk modulus and **(b)** bulk sound velocity at high-P,T conditions. The propagated 1σ uncertainties for K_S and V_Φ are smaller than the sizes of the plotted curves.

832 **Figure 12.** The modeled adiabatic temperature profiles as a function of pressure in both
833 harmonic (dashed) and anharmonic (solid) models. The starting temperature (T_0) at P = 0 GPa is
834 marked for each curve, and the averaged mantle geotherm (Katsura 2022) is plotted as a bold
835 brown curve. The uncertainty for the temperature is exhibited as shaded area if larger than the
836 size of the curve.
837

838 **Table 1.** The fitted parameters for the measured high-*P,T* vibrational frequency (v_i, in the unit of

839 cm^{-1}) according to Eqn (1).

symmetry	v_0 (cm^{-1})	a ($cm^{-1}\cdot K^{-1}$)	b ($cm^{-1}\cdot GPa^{-1}$)	$k \times 10^3$ ($cm^{-1}\cdot GPa^{-1}\cdot K^{-1}$)	assignment
A_g	960.5	-0.020(9)	4.40(6)	0.44(4)	ν_3
B_{3g}	919.9	-0.025(8)	2.58(3)	-0.09(6)	ν_3
A_g	854.6	-0.017(1)	2.82(5)	0.87(5)	$\nu_1+\nu_3$
A_g	823.8	-0.020(7)	2.77(7)	1.17(1)	$\nu_1+\nu_3$
A_g	605.3	-0.016(8)	2.83(4)	0.54(2)	ν_4
B_{1g}	585.8	-0.017(6)	2.24(3)	-0.19(5)	ν_4
A_g	542.7	-0.008(4)	1.75(9)	-0.37(6)	ν_4
B_{3g}	428.5	-0.020(2)	3.88(6)	0.79(4)	ν_2
A_g	321.7	-0.015(2)	3.26(1)	0.33(8)	R(Si)+ T(M)
A_g	300.3	-0.022(2)	3.90(1)	0.29(5)	R(Si)+ T(M)
A_g	222.3	-0.009(6)	1.17(9)	-0.08(4)	R(Si)+ T(M)

840

841

Supplementary figure captions

Figure S1. Configuration of external resistive heating diamond anvil cell.

Figure S2(a-c). Variations of the vibrational frequencies with pressure at high temperatures.

Table S1. The fitted vibrational frequencies (cm^{-1}) for San Carlos olivine at various *P-T* condition.

Table S2. The thermodynamic properties for olivine at high temperatures and high pressures.

Table S3. The averaged anharmonic parameters for different frequency continua in olivine, which are fitted as a 6th-order polynomial function of T at various pressures: a_i (10^{-6} K^{-1}) = $c_1(T/1000)^6 + c_2(T/1000)^5 + c_3(T/1000)^4 + c_4(T/1000)^3 + c_5(T/1000)^2 + c_6(T/1000)$ with $c_0 = 0$ to satisfy that a_i approaches zero at $T = 0$ K.

Pressure (GPa)	c_1	c_2	c_3	c_4	c_5	c_6
Continuum I (103 – 478 cm^{-1})						
0	110.33	-663.89	1558.61	-1795.04	1036.94	-263.66
3	109.92	-661.74	1554.55	-1792.09	1036.83	-264.67
6	109.12	-656.94	1543.61	-1780.53	1031.47	-264.27
9	108.49	-653.28	1535.35	-1771.55	1026.87	-263.65
12	106.91	-644.11	1514.88	-1749.74	1015.92	-261.76
14	106.16	-639.61	1504.59	-1738.56	1010.16	-260.70
Continuum II (499 – 639 cm^{-1})						
0	50.55	-304.89	718.26	-831.99	485.92	-126.88
3	51.11	-308.34	726.70	-842.33	492.45	-128.90
6	51.47	-310.49	731.88	-848.65	496.57	-130.29
9	51.87	-312.97	737.79	-855.62	500.77	-131.55
12	51.84	-312.88	738.01	-856.58	501.98	-132.20

14	51.92	-313.41	739.36	-858.40	503.30	-132.69
Continuum III (822 – 973 cm^{-1})						
0	40.93	-246.06	576.87	-662.84	381.22	-95.67
3	41.58	-250.10	586.73	-674.87	388.79	-98.00
6	42.04	-252.91	593.47	-683.06	394.07	-99.73
9	42.55	-256.00	600.87	-691.81	399.38	-101.32
12	42.64	-256.65	602.85	-694.85	401.83	-102.33
14	42.80	-257.63	605.28	-697.95	403.94	-103.05

Table S4. The fitted slope of dT_S/dP for the adiabatic temperature profile in both harmonic and anharmonic models, and T_0 is the starting temperature at P = 0 GPa

T_0 (K)	$(dT_S/dP)_{\mathbf{har}}$ (K/GPa)	$(dT_S/dP)_{\mathbf{anh}}$ (K/GPa)
300	2.2563	2.2136
400	2.9475	2.8866
500	3.6361	3.5523
600	4.3361	4.2231
700	5.0592	4.9092
800	5.8152	5.6189
900	6.6119	6.3585
1000	7.4544	7.1320
1100	8.3456	7.9407
1200	9.2851	8.7832
1300	10.2695	9.6551
1400	11.2916	10.5486
1500	12.3402	11.4521
1600	13.3999	12.3502
1700	14.4507	13.2234
1800	15.4678	14.0482
1900	16.0370	14.4274
2000	16.8523	15.0312

Figure 1

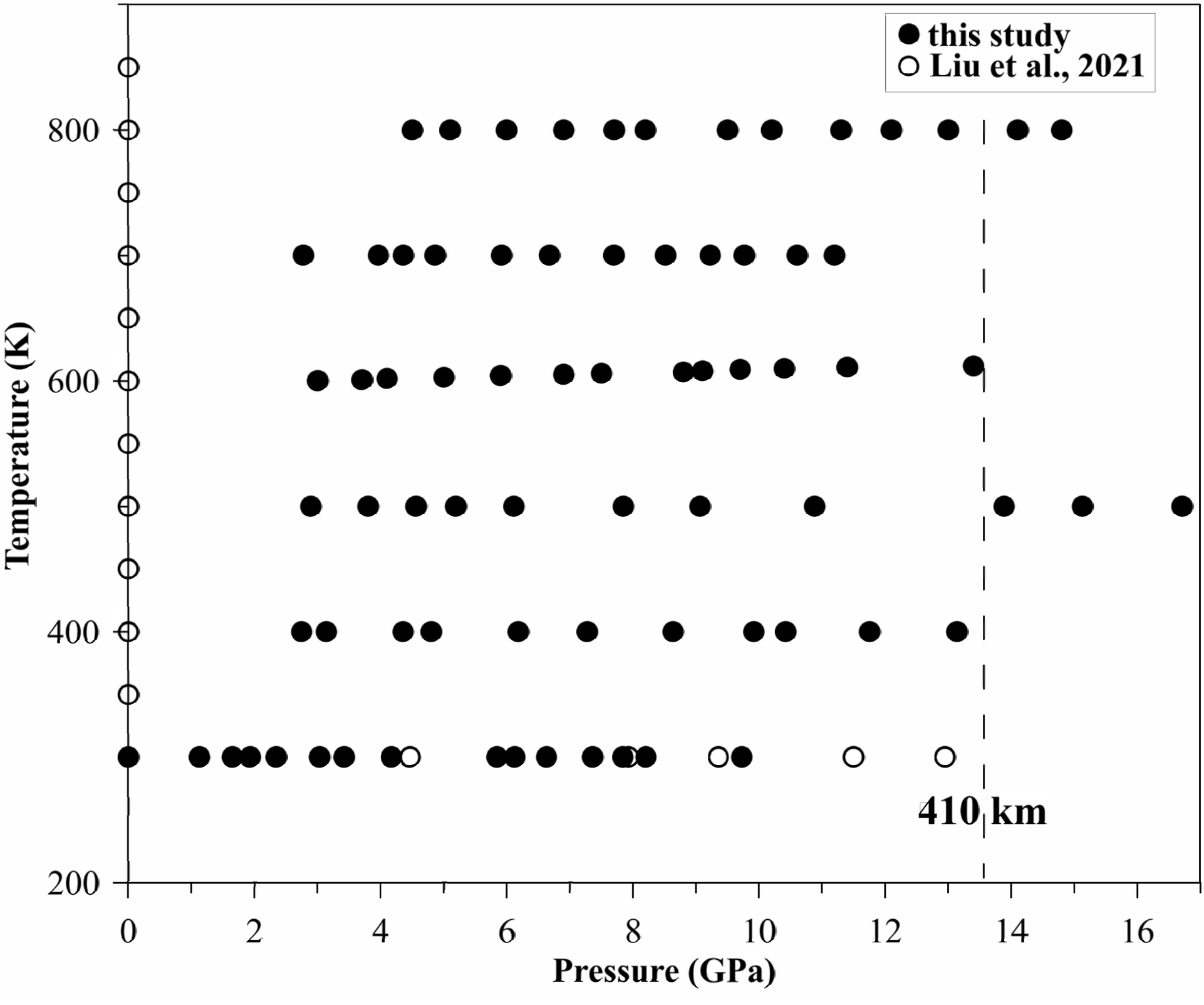
this study
Liu et al., 2021
410 km
Temperature (K)
Pressure (GPa)
200
400
600
800
0
2
4
6
8
10
12
14
16

Figure 2

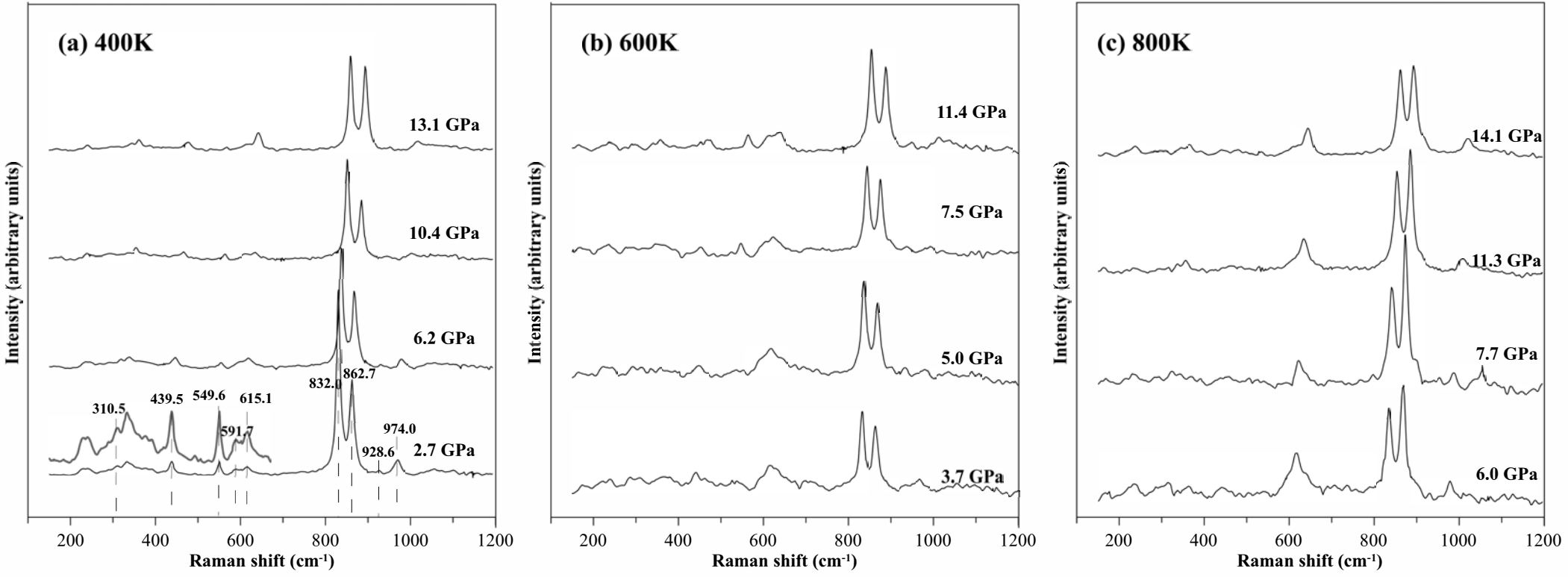
(a) 400K
13.1 GPa
10.4 GPa
6.2 GPa
2.7 GPa
310.5
439.5
549.6
615.1
591.7
832.0
862.7
928.6
974.0
Intensity (arbitrary units)
Raman shift (cm-1)
(b) 600K
11.4 GPa
7.5 GPa
5.0 GPa
3.7 GPa
Intensity (arbitrary units)
Raman shift (cm-1)
(c) 800K
14.1 GPa
11.3 GPa
7.7 GPa
6.0 GPa
Intensity (arbitrary units)
Raman shift (cm-1)

Figure 3

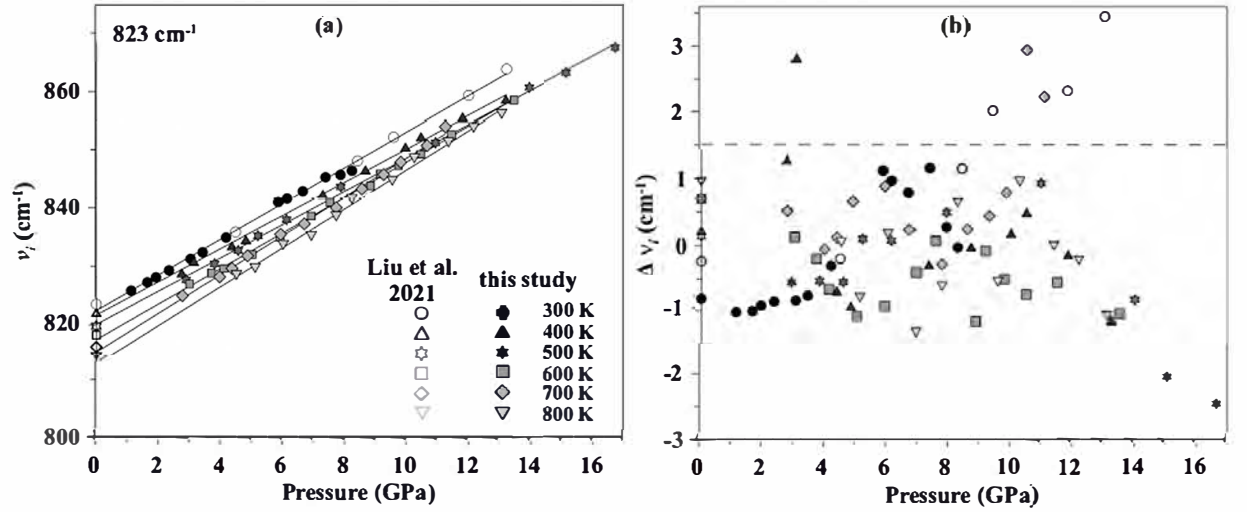
823 cm-1
(a)
860
840
820
800
νi (cm-1)
0
2
4
6
8
10
12
14
16
Pressure (GPa)
Liu et al. 2021
this study
300 K
400 K
500 K
600 K
700 K
800 K
(b)
3
2
1
0
-1
-2
-3
Δ νi (cm-1)
0
2
4
6
8
10
12
14
16
Pressure (GPa)

Figure 4

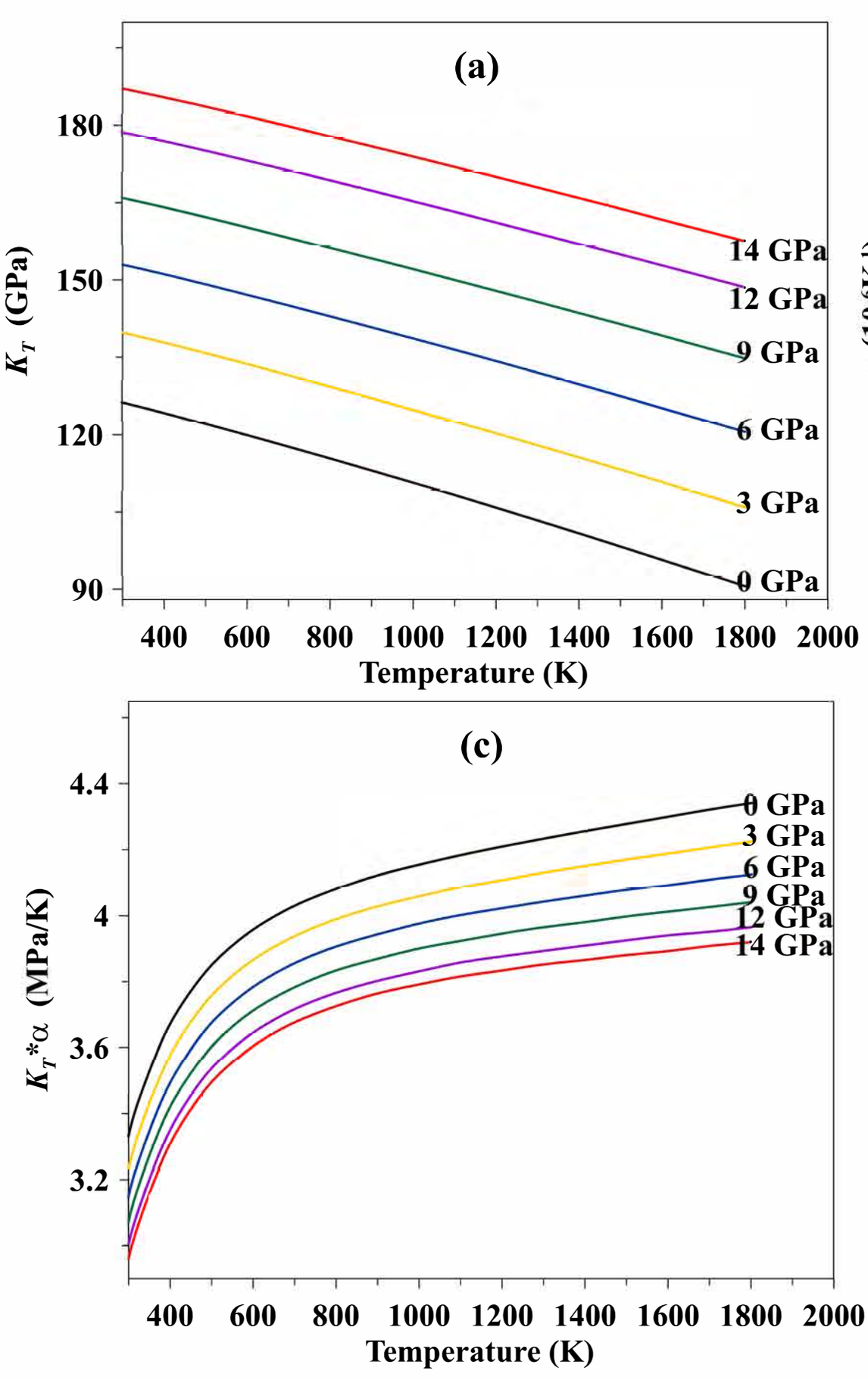
(a)
180
150
120
90
K_T (GPa)
14 GPa
12 GPa
9 GPa
6 GPa
3 GPa
0 GPa
400 600 800 1000 1200 1400 1600 1800 2000
Temperature (K)

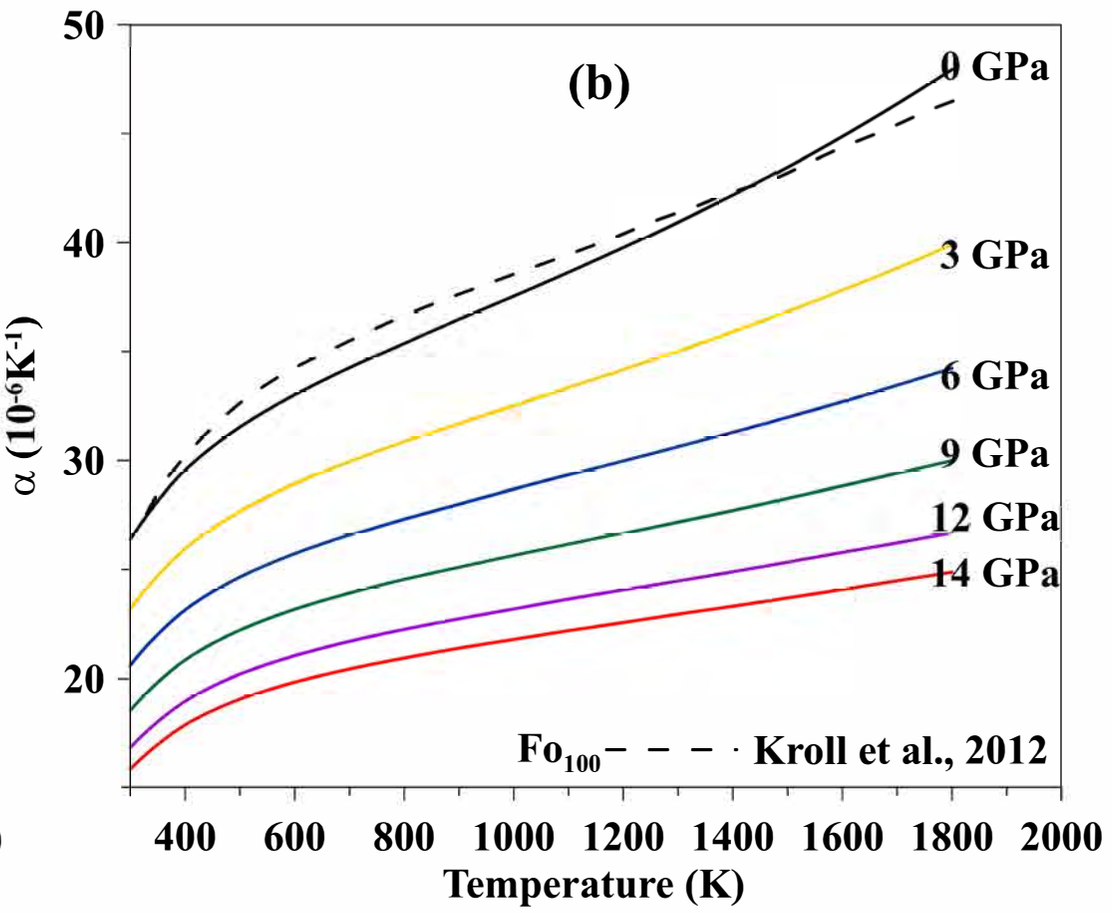
(b)
50
40
30
20
α (10^{-6}K^{-1})
0 GPa
3 GPa
6 GPa
9 GPa
12 GPa
14 GPa
Fo$_{100}$ – – – Kroll et al., 2012
400 600 800 1000 1200 1400 1600 1800 2000
Temperature (K)

(c)
4.4
4
3.6
3.2
K_T*α (MPa/K)
0 GPa
3 GPa
6 GPa
9 GPa
12 GPa
14 GPa
400 600 800 1000 1200 1400 1600 1800 2000
Temperature (K)

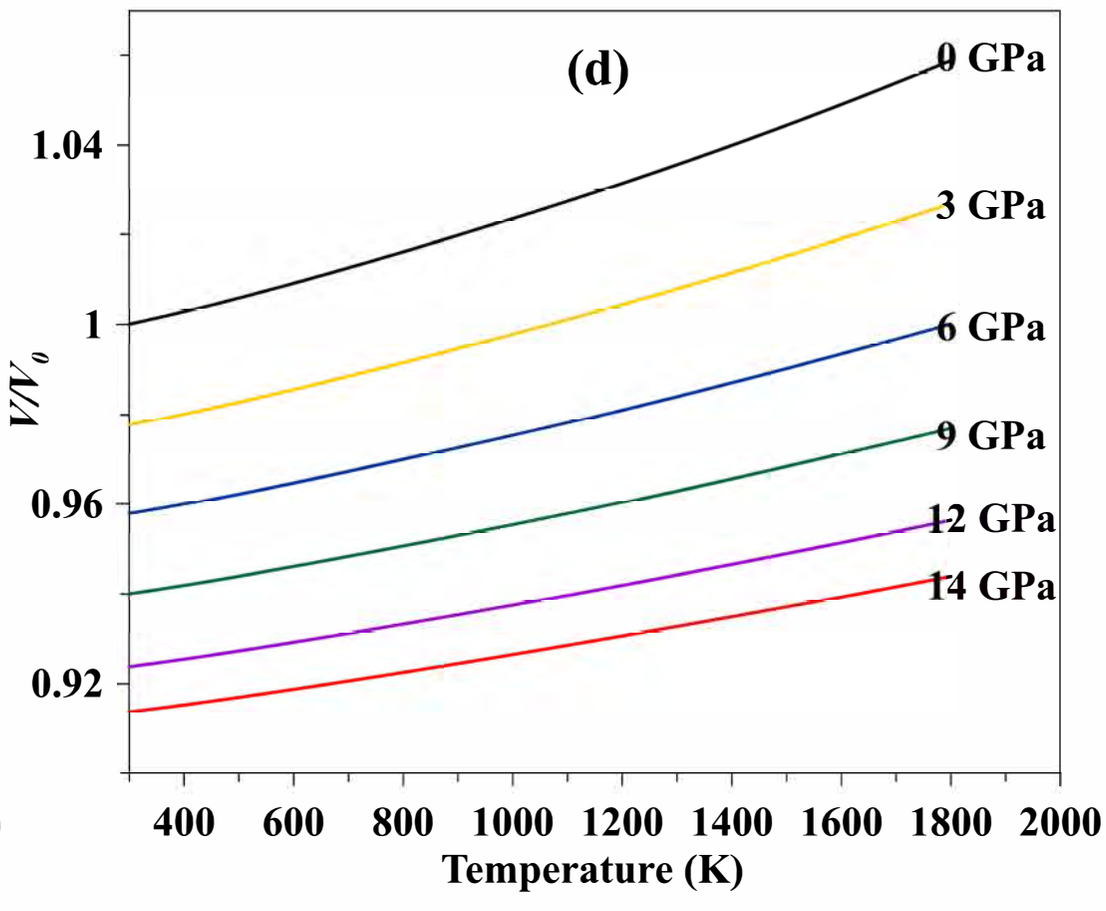
(d)
1.04
1
0.96
0.92
V/V$_0$
0 GPa
3 GPa
6 GPa
9 GPa
12 GPa
14 GPa
400 600 800 1000 1200 1400 1600 1800 2000
Temperature (K)

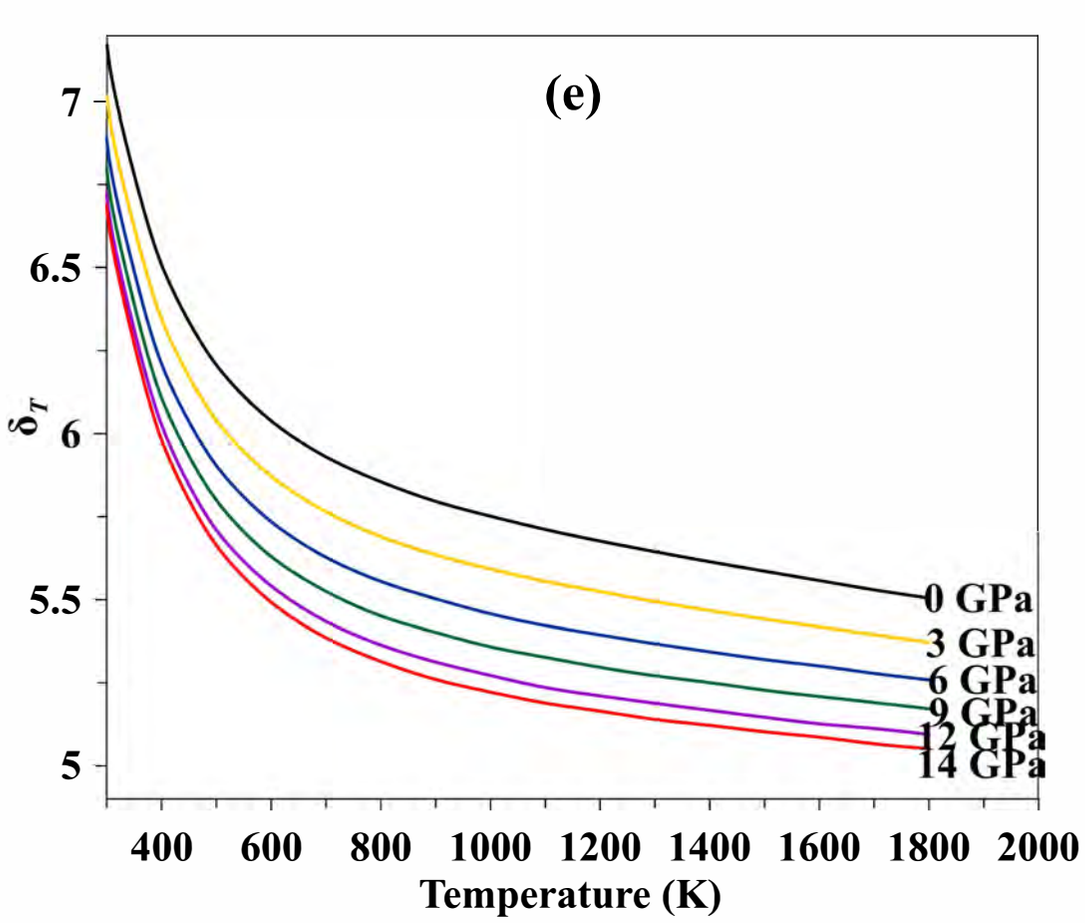
(e)
7
6.5
6
5.5
5
δ_T
0 GPa
3 GPa
6 GPa
9 GPa
12 GPa
14 GPa
400 600 800 1000 1200 1400 1600 1800 2000
Temperature (K)

Figure 5

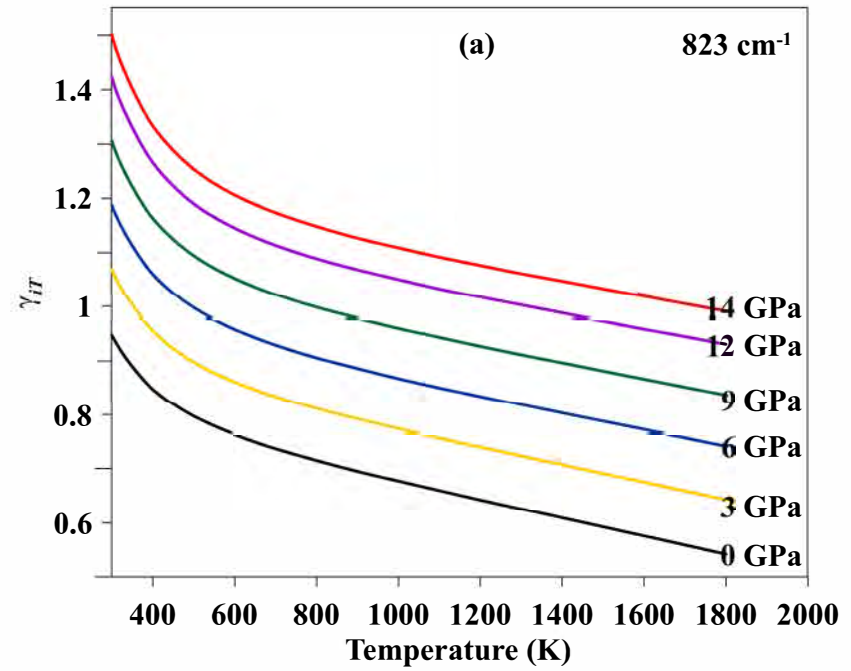
(a)
823 cm-1
1.4
1.2
1
0.8
0.6
γiT
14 GPa
12 GPa
9 GPa
6 GPa
3 GPa
0 GPa
400 600 800 1000 1200 1400 1600 1800 2000
Temperature (K)

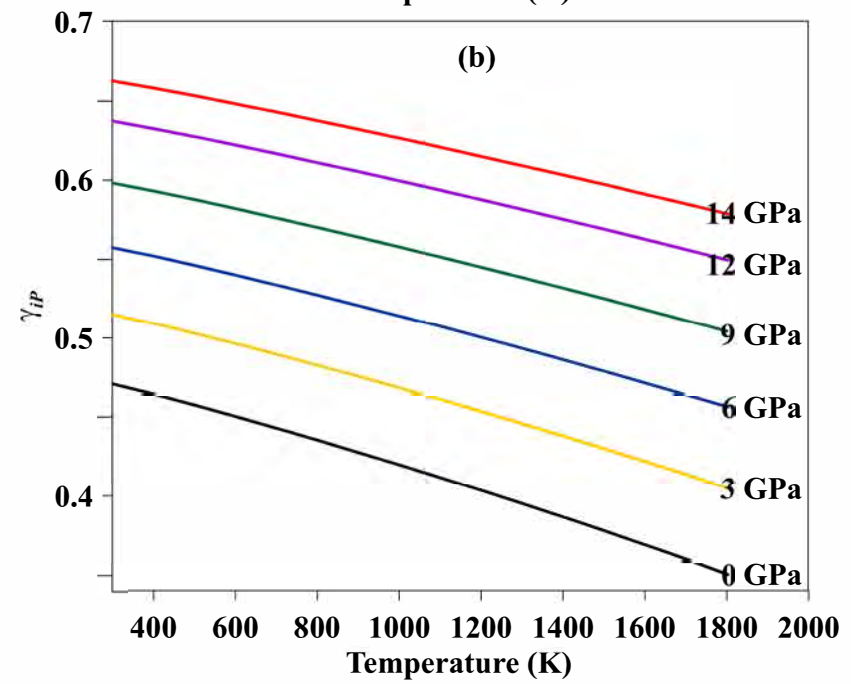
(b)
0.7
0.6
0.5
0.4
γiP
14 GPa
12 GPa
9 GPa
6 GPa
3 GPa
0 GPa
400 600 800 1000 1200 1400 1600 1800 2000
Temperature (K)

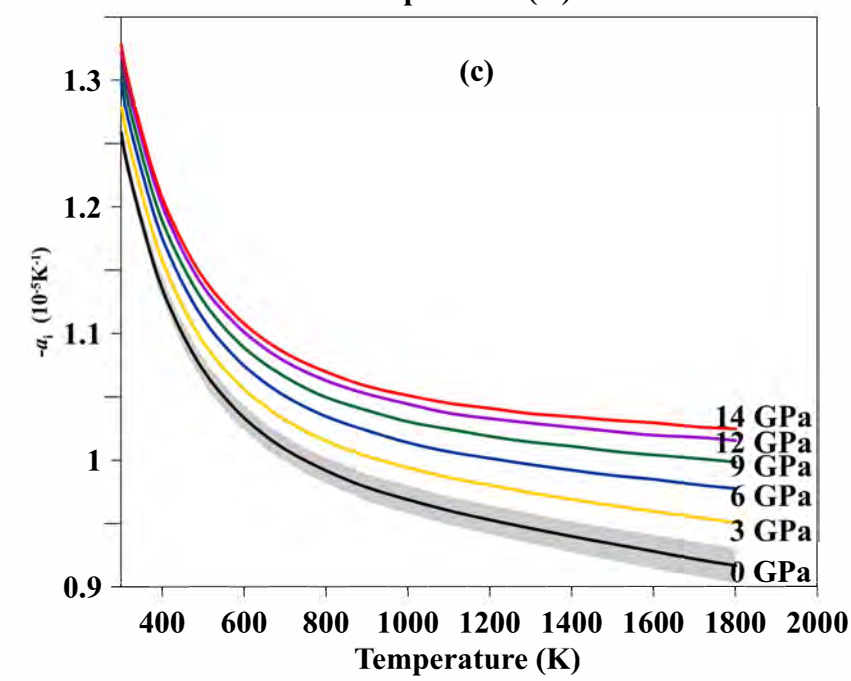
(c)
1.3
1.2
1.1
1
0.9
-αi (10-5K-1)
14 GPa
12 GPa
9 GPa
6 GPa
3 GPa
0 GPa
400 600 800 1000 1200 1400 1600 1800 2000
Temperature (K)

Figure 6

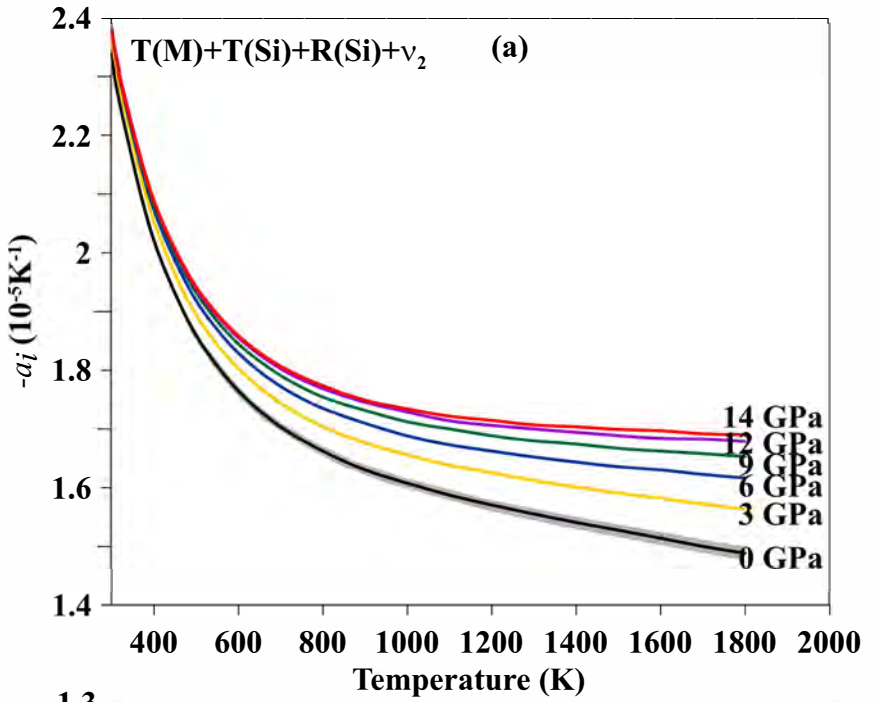
T(M)+T(Si)+R(Si)+ν2
(a)
-ai (10-5K-1)
2.4
2.2
2
1.8
1.6
1.4
14 GPa
12 GPa
9 GPa
6 GPa
3 GPa
0 GPa
400
600
800
1000
1200
1400
1600
1800
2000
Temperature (K)

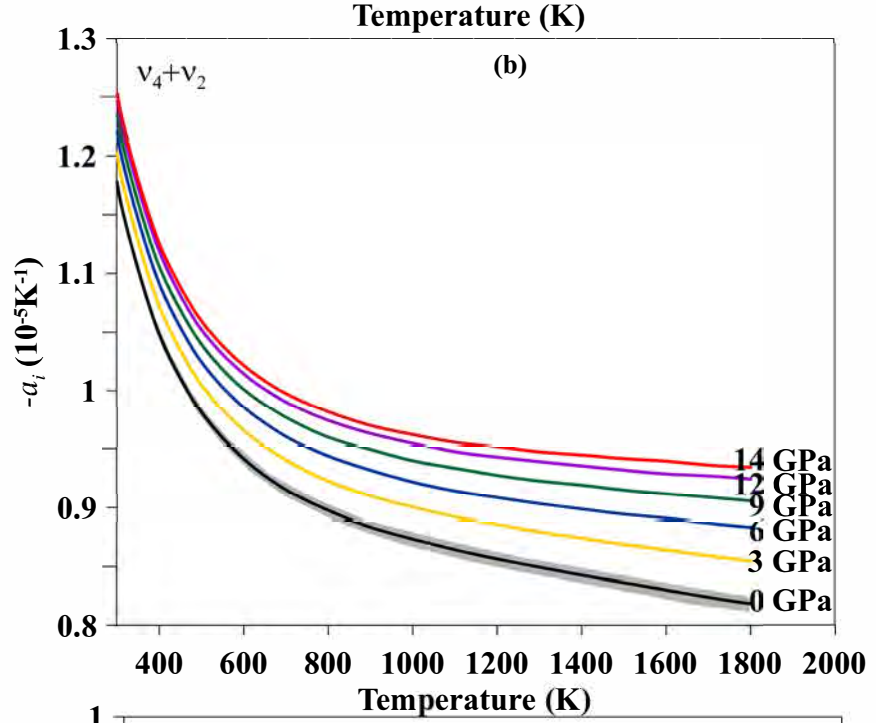
ν4+ν2
(b)
-ai (10-5K-1)
1.3
1.2
1.1
1
0.9
0.8
14 GPa
12 GPa
9 GPa
6 GPa
3 GPa
0 GPa
400
600
800
1000
1200
1400
1600
1800
2000
Temperature (K)

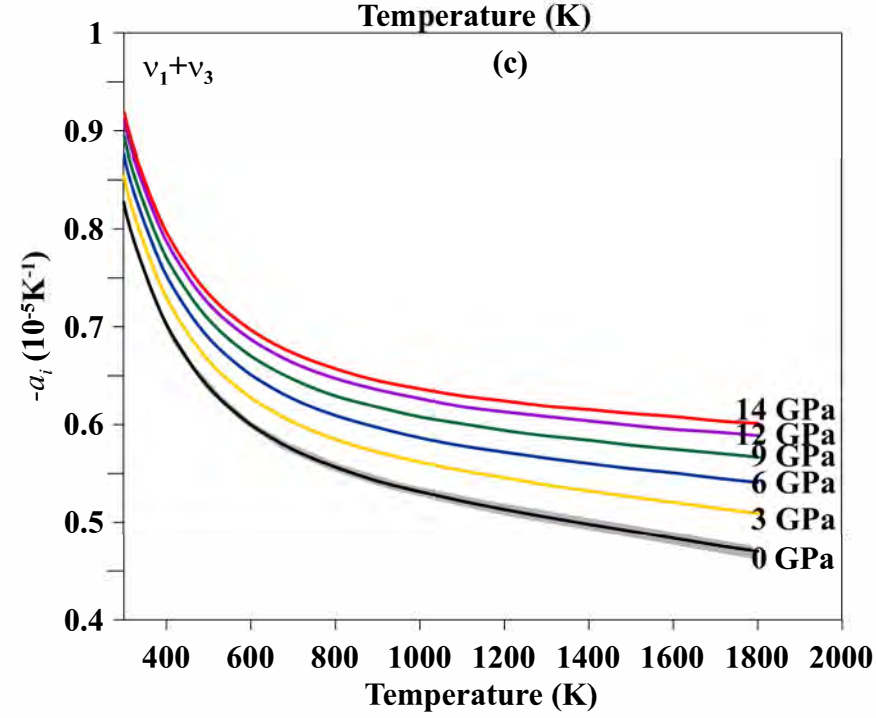
ν1+ν3
(c)
-ai (10-5K-1)
1
0.9
0.8
0.7
0.6
0.5
0.4
14 GPa
12 GPa
9 GPa
6 GPa
3 GPa
0 GPa
400
600
800
1000
1200
1400
1600
1800
2000
Temperature (K)

Figure 7

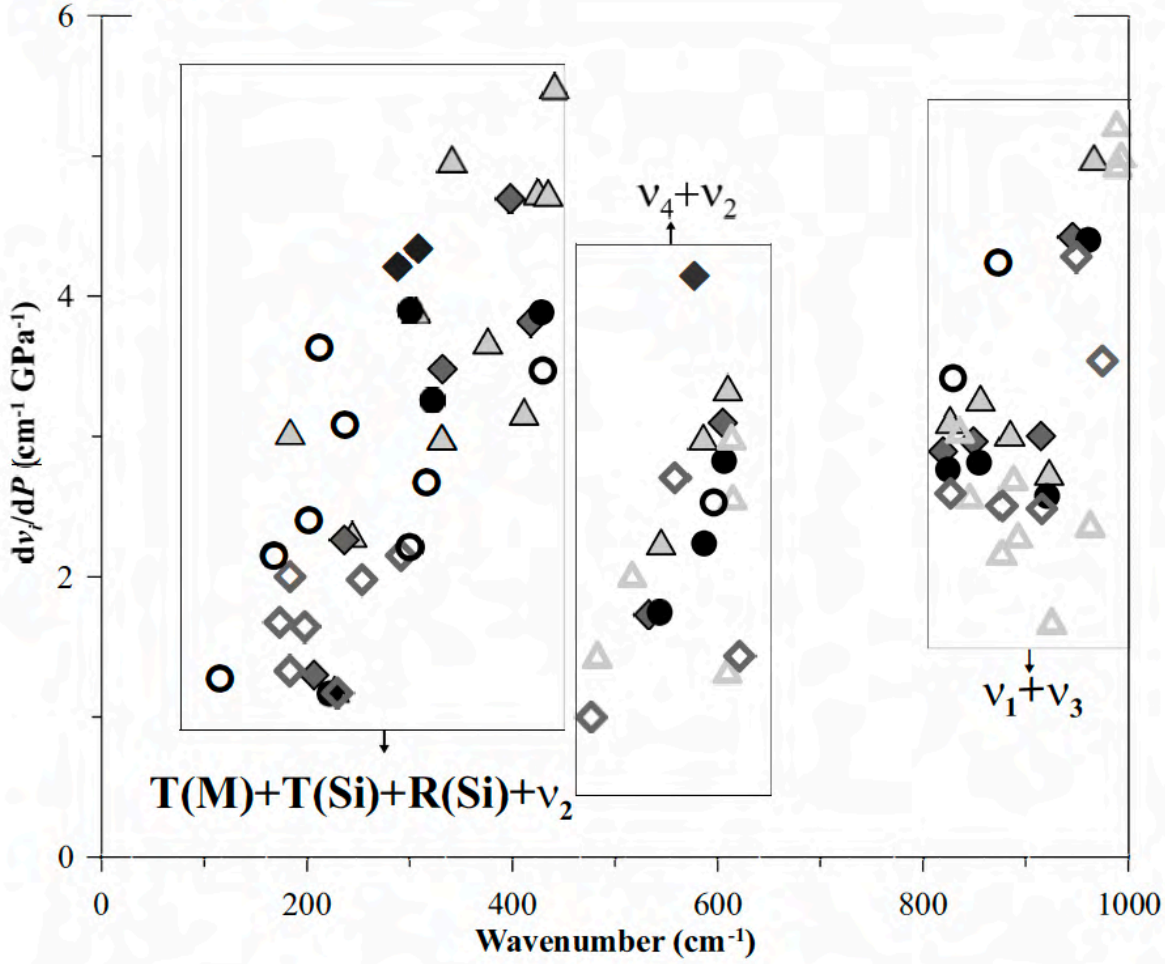

Raman Active Modes

- Fo_{100} (Choeals 1990)
- $Fo_{58}Fa_{42}$ (Liu et al. 2021)
- $Fo_{89}Fa_{11}$ (this study)

IR Active Modes

- Fo_{100} (Wang et al. 1993; Hofmeister et al. 1989)
- Fa_{100} (Hofmeister et al. 1989)
- $CaMgSiO_4$ (Hofmeister et al. 1997)

Figure 8

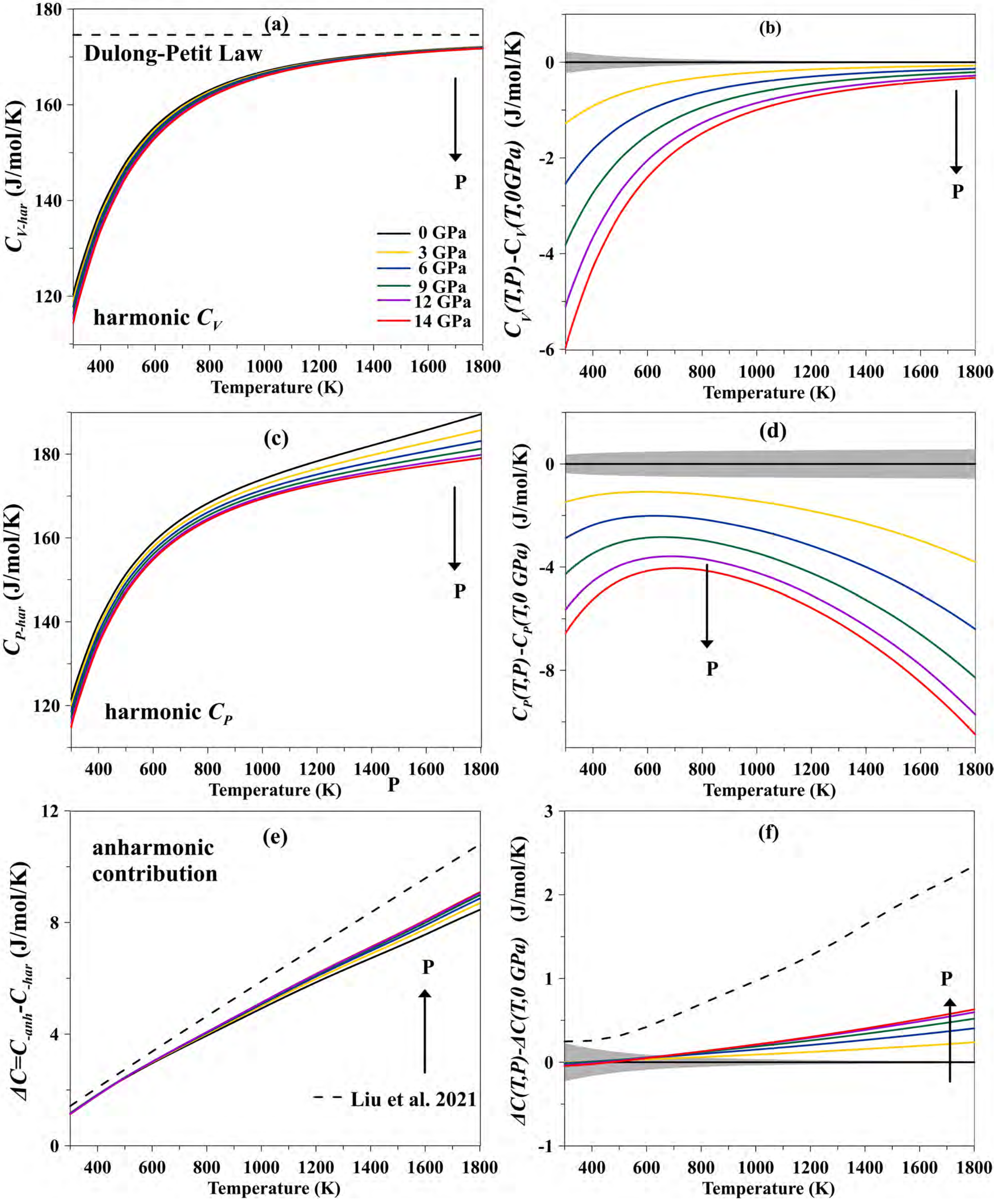
(a)
Dulong-Petit Law
harmonic C_V
$C_{V\text{-}har}$ (J/mol/K)
P
0 GPa
3 GPa
6 GPa
9 GPa
12 GPa
14 GPa
Temperature (K)
(b)
$C_V(T,P)$-$C_V(T,0GPa)$ (J/mol/K)
P
Temperature (K)
(c)
harmonic C_P
$C_{P\text{-}har}$ (J/mol/K)
P
Temperature (K)
(d)
$C_P(T,P)$-$C_P(T,0\ GPa)$ (J/mol/K)
P
Temperature (K)
(e)
anharmonic contribution
ΔC=$C_{\text{-}anh}$-$C_{\text{-}har}$ (J/mol/K)
P
Liu et al. 2021
Temperature (K)
(f)
$\Delta C(T,P)$-$\Delta C(T,0\ GPa)$ (J/mol/K)
P
Temperature (K)

Figure 9

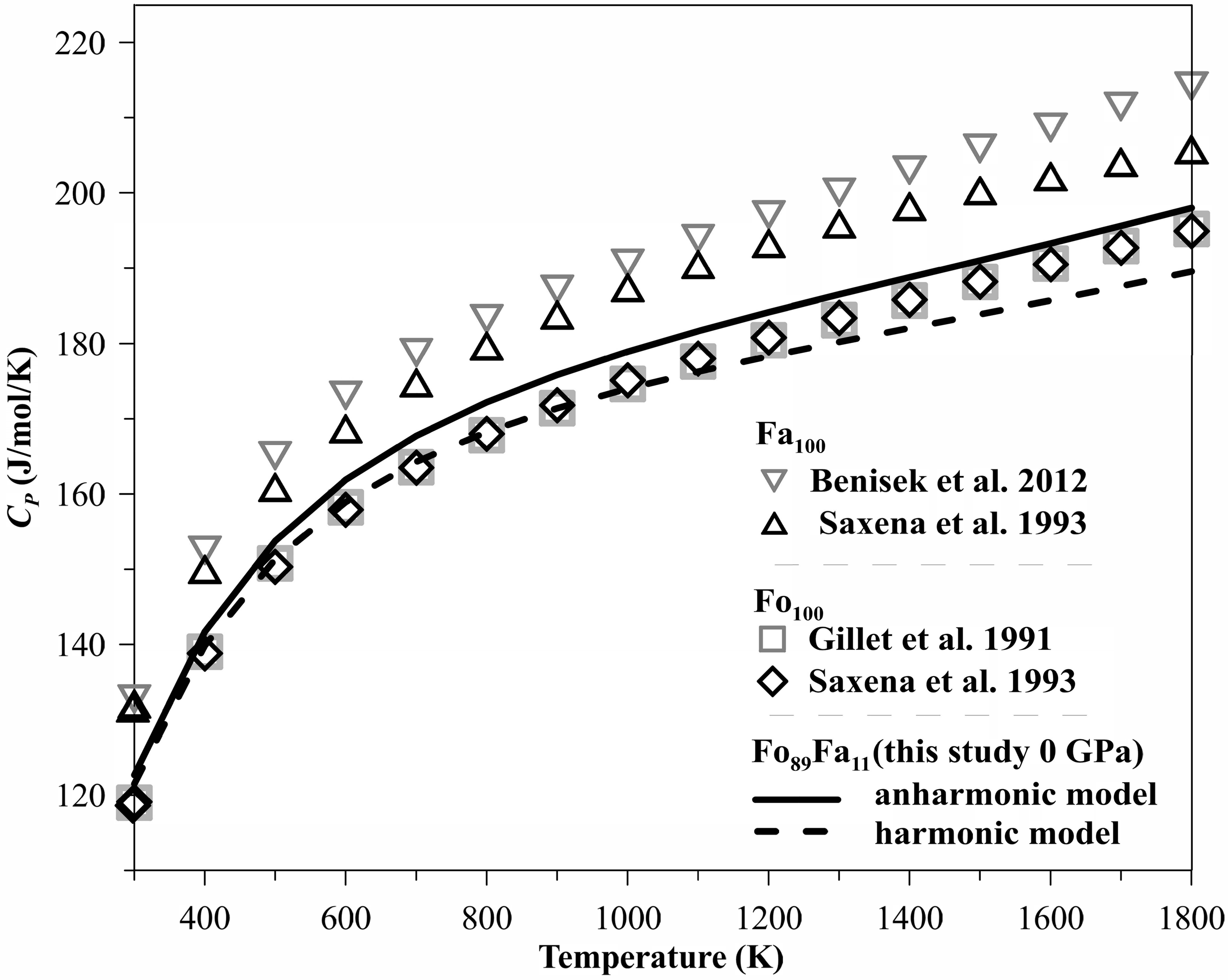
220
200
180
160
140
120
C_P (J/mol/K)
400
600
800
1000
1200
1400
1600
1800
Temperature (K)
Fa_{100}
Benisek et al. 2012
Saxena et al. 1993
Fo_{100}
Gillet et al. 1991
Saxena et al. 1993
$Fo_{89}Fa_{11}$(this study 0 GPa)
anharmonic model
harmonic model

Figure 10

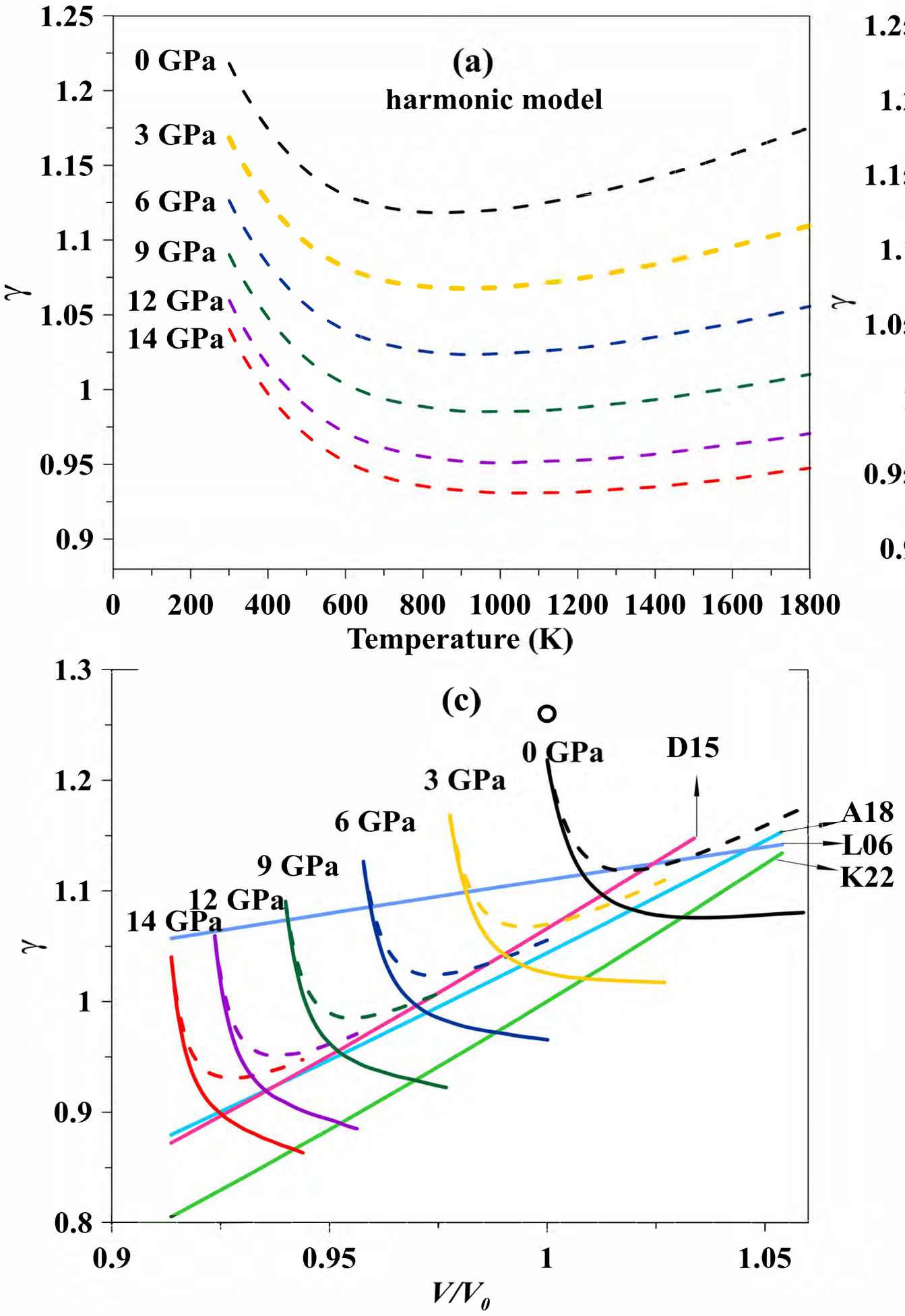

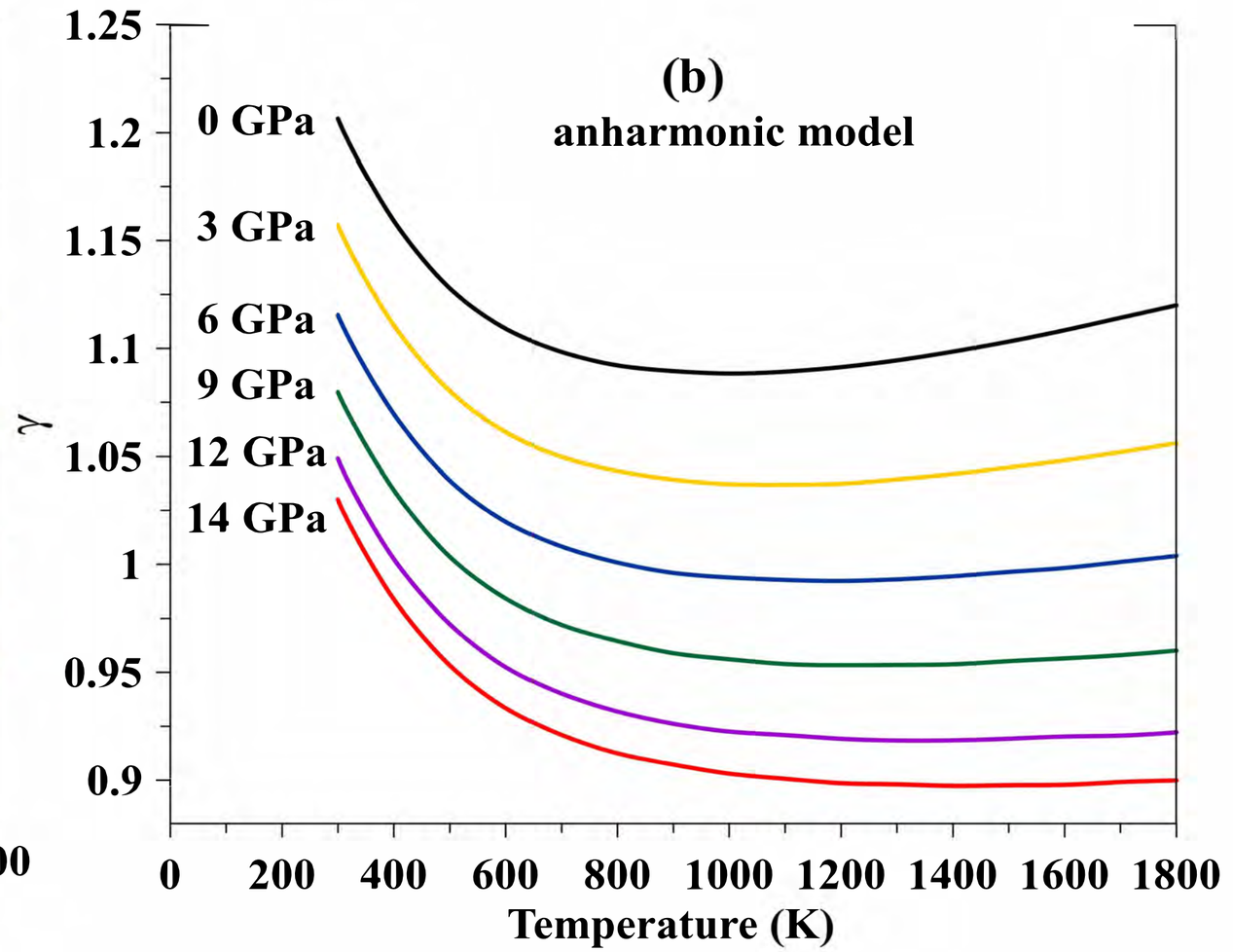

$Fo_{90}Fa_{10}$ ○ Isaak 1992

L06 Liu and Li 2006

A18 Angel et al. 2018

K22 Katsura 2022

Fo_{100} D15 Dorogokupets et al. 2015

Figure 11

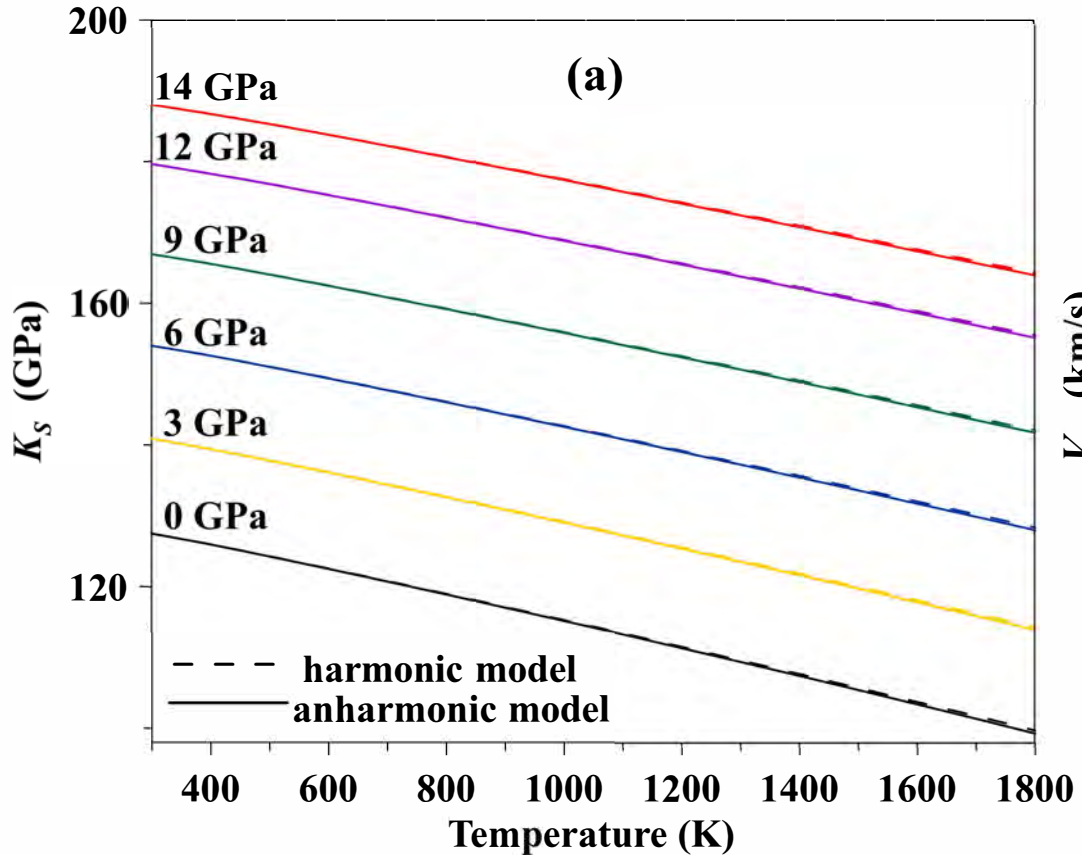
(a)
14 GPa
12 GPa
9 GPa
6 GPa
3 GPa
0 GPa
harmonic model
anharmonic model
K_S (GPa)
200
160
120
400
600
800
1000
1200
1400
1600
1800
Temperature (K)

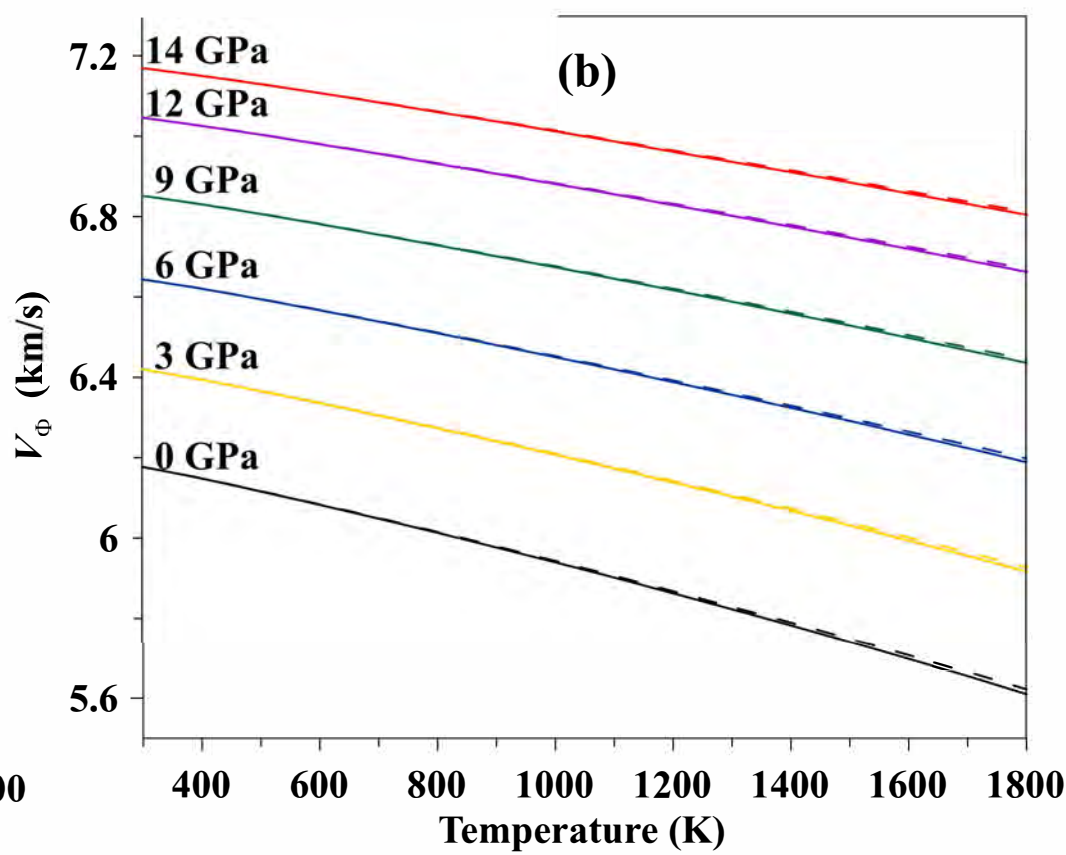
(b)
14 GPa
12 GPa
9 GPa
6 GPa
3 GPa
0 GPa
V_Φ (km/s)
7.2
6.8
6.4
6
5.6
400
600
800
1000
1200
1400
1600
1800
Temperature (K)

Figure 12

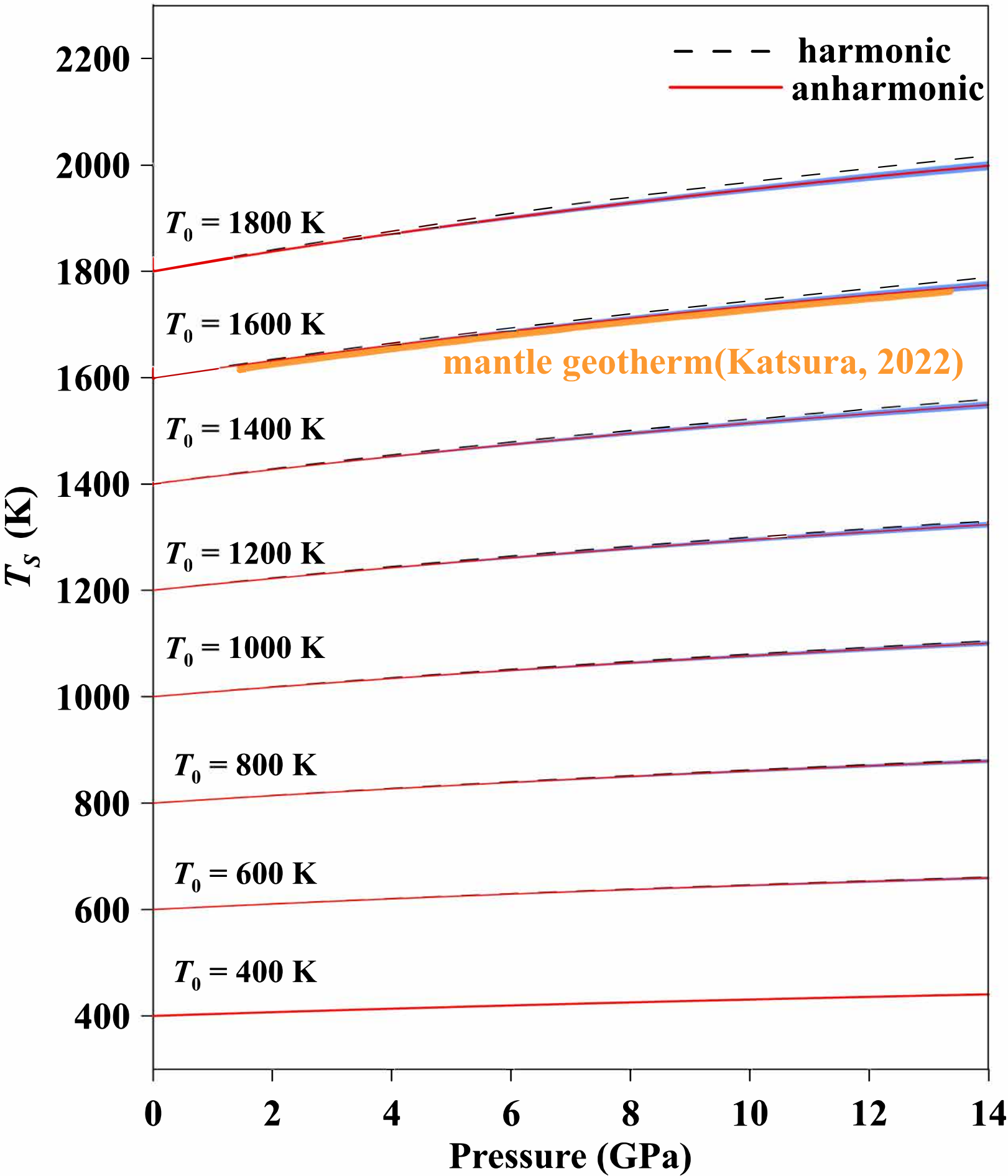
harmonic
anharmonic
T_0 = 1800 K
T_0 = 1600 K
T_0 = 1400 K
T_0 = 1200 K
T_0 = 1000 K
T_0 = 800 K
T_0 = 600 K
T_0 = 400 K
mantle geotherm(Katsura, 2022)
T_S (K)
2200
2000
1800
1600
1400
1200
1000
800
600
400
0
2
4
6
8
10
12
14
Pressure (GPa)